International Journal of Material Science (IJMSCI) Volume 4 Issue 2, June 2014 www.ij-ms.org
doi: 10.14355/ijmsci.2014.0402.05

Low Temperature Ageing Effects in NiTi Shape Memory Alloys

K. Hari Krishnan[1], P. S. Misra[1], K. Chandra[1], Vinod S. Agarwala[2]

[1]Metallurgical and Materials Engineering Department, IIT Roorkee, Roorkee-247 667, India

[2]Air Vehicle Engineering Department, Naval Air Systems Command, United States Navy, Patuxent River, Maryland, USA (Ret.)

hari_gce@yahoo.co.in

Received 31 January, 2014; Revised 2 March, 2014; Accepted 5 April, 2014; Published 20 June, 2014

Abstract

This paper reports the comprehensive study of the characteristics of the R-phase transformations observed in low temperature aged (@ 150^{0}C) Ti-49.85 atomic percent Ni shape memory alloys (SMAs). The stabilizations of the R-phase transformations occurred with two separate transformation peaks were observed in DSC study in prolonged aged conditions. In conventional ageing temperature ageing at 300^{0}C, R-phase transformations exhibit an increase in A_f temperature; but in low temperature aged NiTi shows that measured A_f temperature is lower than the solutionized sample and R-phase appeared well below the original B2→B19′ transformation temperature initially; this result is very peculiar for this ageing treatment. The energy required for the nucleation of this phase $\Delta H_{B19'\rightarrow R}$ on heating cycle was 2.24 J/g, which was much lower than the reverse transformation (on cooling) $\Delta H_{B19'\rightarrow R} = -12.6$ J/g. This loss of about –8.55 J/g, is believed to be covered by the transformations between the two peaks of B19′→R and R→B2 in heating. The occurrence of the R-phase transformation is attributed to precipitation-induced inhomogeneity of the matrix, both in terms of composition and internal stress fields.

Keywords

Austenitic Start (A_s); Martensitic Start (M_s); Austenitic Finish (A_f), Martensitic Finish (A_f); Endothermic Energy; Shape Memory Effect and R-phase Transformations

Introduction

In NiTi Shape memory alloys, transformation temperature is very sensitive to composition. This high composition sensitivity of the transformation temperature is undesirable in most cases since it simply means that very precise composition control of the alloy is necessary in order to get desired transformation temperature properties. This is technically difficult in most cases. It is ideal to have an alloy system whose transformation temperature is insensitive to composition; it is even better to have a way to adjust transformation temperature after the alloy has been produced. There is a very good way to adjust the transformation temperature of TiNi alloys for Ni-rich alloys even after the alloys have been made. It was observed that there is an alternating change in transformation temperatures (R_s and M_s) when Ni-rich TiNi alloy is alternatively aged between two aging temperatures, and the transformation temperature seems to be controlled by aging treatment alone - essentially independent of the number of cycles. Equiatomic TiNi does not show this behavior. This work provides a new way to newly tune the transformation temperature just by changing aging temperature. But the reason for such an interesting behavior was unclear. However, it was realized that such a behavior stems from the equilibrium between TiNi phase and Ni_4Ti_3. Alternating aging treatment between two aging temperatures causes an alternating (reversible) change in B2 matrix composition. Such an alternating change in B2 composition naturally causes an alternating change in R_s and M_s temperature as M_s is also dependent on the size and density of Ni_4Ti_3 precipitates and which are dependent on the number of cycles. Therefore, the key idea in the above is to use the precipitation reaction of the quenched supersaturated TiNi solid solution to newly adjust the composition of the TiNi matrix and create a precise control of transformation temperature. The principle behind this method is the (metastable)-equilibrium

between TiNi and Ni_4Ti_3 precipitates. Although Ni_4Ti_3 is considered as a metastable phase compared with the equilibrium $TiNi_3$ precipitate, it is quite stable at temperature below 600^{0}C and under normal aging condition only Ni_4Ti_3 is observed. When precipitation reaction occurs, formation of Ni_4Ti_3 precipitates is accompanied by a decrease in Ni content of the TiNi matrix, thus the result, R_s and M_s temperatures. Higher aging temperature causes higher Ni content in the TiNi matrix and consequently leads to lower transformation temperatures; lower aging temperature produces a TiNi matrix of lower Ni content and consequently leads to higher transformation temperatures. This present paper deals with the comprehensive investigations of the R-phase transformations observed in the low temperature ageing treatment, i.e. aged at 150^{0}C.

Experimental

The shape memory NiTi alloys were obtained from Naval Air Systems Command, U.S. Navy in 12.5 mm diameter rod form. The final thickness of 0.5 mm (as a sheet form) was achieved by hot rolling followed by cold rolling. Thereafter samples were cut into the dimensions for 15×5×0.5 mm. The cut specimens were subjected to the normalizing treatment at 500°C (773 K) for 1 hour in tube furnace followed by water quenching. Then the NiTi shape memory sheet samples were solutionized at 850^{0}C for one hour in tube furnace in an argon atmosphere and quenched to room temperature. Then the samples were subjected to the ageing treatment at 150^{0}C for different ageing intervals of 0, 4, 24 and 72 hrs. The transformation behavior and their characteristic temperatures were determined using a DSC cell (Perkins, pyris diamond) with the specimen weight between 15 mg to 25 mg. In DSC tests, specimen was heated up to 150^{0}C with heating rate of 10 K/minute and held 5 minutes to obtain thermal equilibrium, followed by cooled down to room temperature.

Results

The specimen in the as-quenched condition exhibited single-step transformation between B2 (austenitic, cubic) and B19′ monoclinic martensite, during both cooling as well as heating as shown in Fig.1. This because as quenched samples do not possess R-phase transformations. The endothermic energy required for the formations of the B2 phase in the forward transformation ($\Delta H_{M\rightarrow A}$), was +7.32 J/g, lower than the exothermic energy required ($\Delta H_{A\rightarrow M}$) for the formations of the B19′ phase in the reverse transformations. The similar results were observed in aged 4h (as shown in Fig. 2) and 24 h (as shown in Fig. 3) NiTi samples, and there were no major changes recorded in M_p temperature. But greater variations were observed in M_s and M_f temperatures; it may be due to the continuous fluctuations in the chemical compositions distributions during ageing treatment. The 72 hours aged NiTi sample exhibited two-step transformations in heating as well as cooling. The first transformation step on heating (low temperature transformation peak), and the first transformation peak on cooling (high temperature transformation peak) was related with the R-phase transformations. There was the separate R- transformation step recorded, with 16^{0}C transformation thermal hysteresis ($\Delta R=R_f-R_s$) on the heating cycle, while upon cooling, R-phase transformations emerged along with the B19′ phase, and the transformation thermal hysteresis ($\Delta R=R_f-R_s$) observed in this phase was at 11^{0}C.

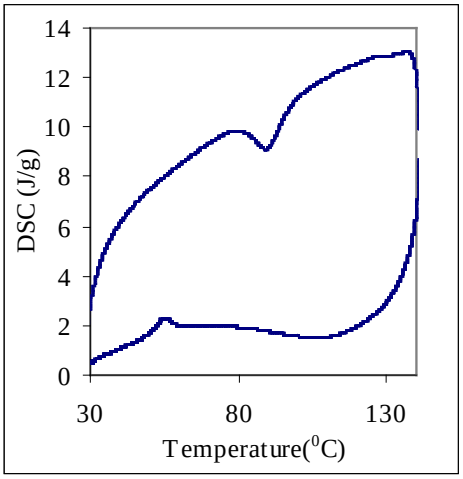

FIG. 1- DSC PLOT OF THE NITI SOLUTIONIZED AT 850^{0}C FOR 1 HOUR.

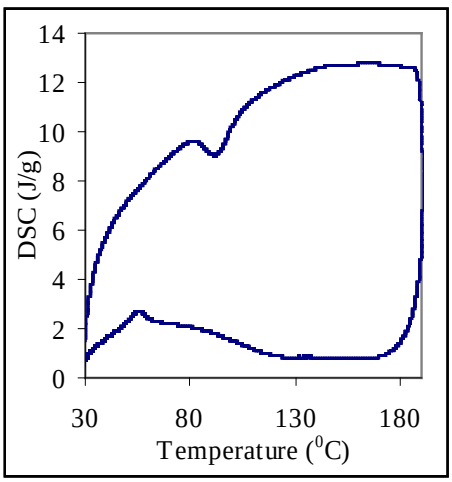

FIG. 2 - DSC PLOT OF THE NITI AGED AT 150^{0}C FOR 4 HOURS.

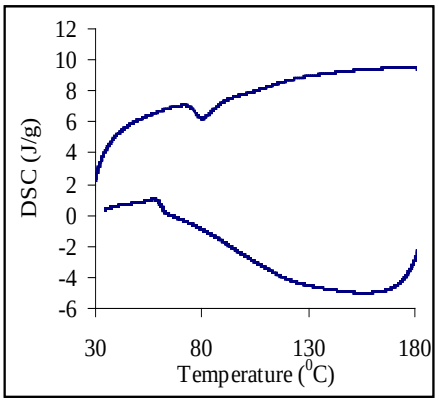

FIG. 3- DSC PLOT OF THE NITI AGED AT 150⁰C FOR 24 HOURS

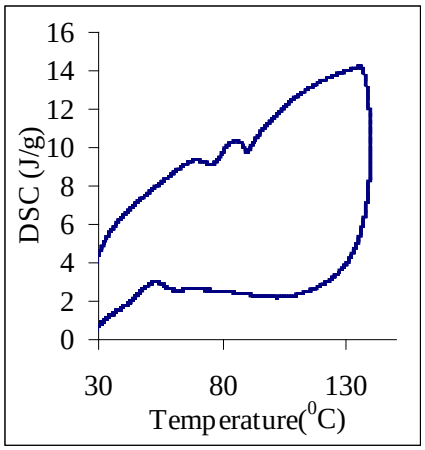

FIG. 4 - DSC PLOT OF THE NITI AGED AT 150⁰C FOR 72 HOURS

Discussions

As the solutionized NiTi sample showed the first order martensitic transformations, it was studied as follows T_0= ½ (Ms+Af)/2 = (77+114)/2 = 95.5⁰C, T_0 >As, 77 ⁰C. From the above figures the T_0 (T_0>Ms) value, studied from the DSC plot, it was concluded that, it follows the first order martensitic transformations. Fig. 5 shows the effect of ageing time on A_s, A_p, and A_f temperatures. The solutionized specimen show high A_f temperature rather than aged samples, and aged 72 hrs sample shows higher A_s temperature than solutionized condition. Based on the literature reports, if the sample exists with the R-phase transformations, it should possess higher A_f temperature, but this R-phase ageing treatment shows different behaviors. The R-phase transformations involve decreases in M_s temperature as compared to the aged for 4 and 24 hours, but equals to the solutionized NiTi sample, which is as shown in Fig. 6. Thermal hysteresis required for the formations for the M (M_f - M_s) and A (A_f - A_s) transformations is lesser in aged for 72 hrs (exists along with R-phase transformations) and even lesser than the solutionized sample, which is shown in Fig. 7. The effect of ageing time on enthalpy changes are shown in Fig. 8. The endothermic energy required for the formations of the B2 phase was 7.32 J/ g, which is much lesser than the energy required for the formations of the B19′ phase, -13.3 J/g. It means that the higher lattice distortions required for the formations of the B19′ (monoclinic martensite) transformations from the B2 phase. The remaining exothermic energy, –6 J/g, is involved in the formations of the heavy distortions in B19′ phase. The energy required for nucleation of the B19′ phase in 72 hrs aged sample has –13.3 J/g, a combined energy of the $\Delta H_{B19'}$ +ΔH_{B2} phases is 6.32 J/g much higher than the B2 phase transformations (ΔH_{B2} = 4.05 J/g), this loss of about the remaining exothermic energy around –8.55 J/g involved in the nucleation of the R-phase transformations, from this value around 2.27 J/g involved in the formations of the R-phase transformations in the heating forward (heating cycle) transformations. The remaining energy required to the creation of the local stresses and heavy distortions occurred in the B19′phase transformations. The transformations thermal hysteresis η = A_f- M_s is lesser in the case of aged for 24 hrs sample as compared to the solutionized and the aged for 72 hrs NiTi sample, mentioned in Fig. 9.

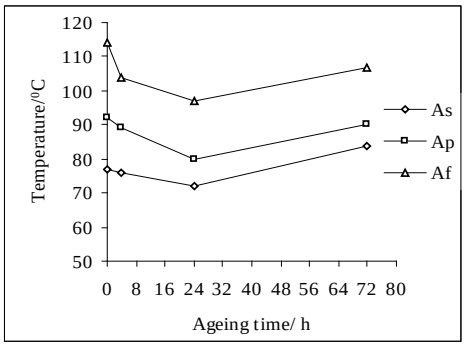

FIG. 5 - COMPARATIVE STUDY OF THE CHARACTERISTICS OF AGING TIME ON A_s, A_p, AND A_f TEMPERATURES

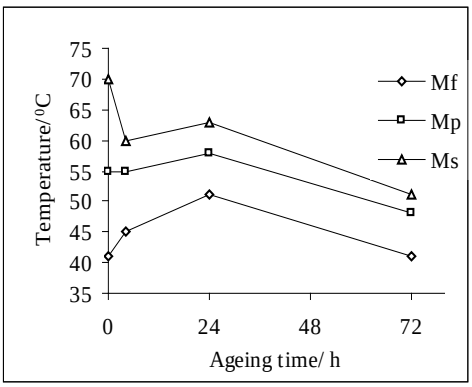

FIG.6 - COMPARATIVE STUDY OF THE CHARACTERISTICS OF AGING TIME ON M_S, M_P, AND M_F TEMPERATURES.

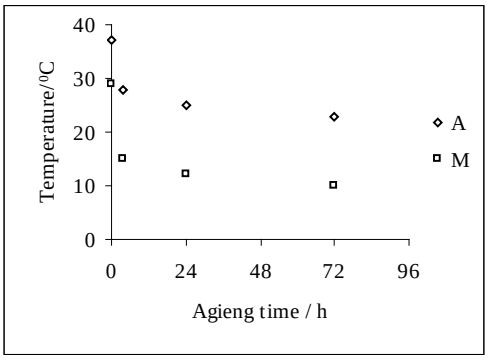

FIG.7 - EFFECT OF AGEING TIME ON M (M_F-M_S) AND A (A_F- A_S) TEMPERATURES

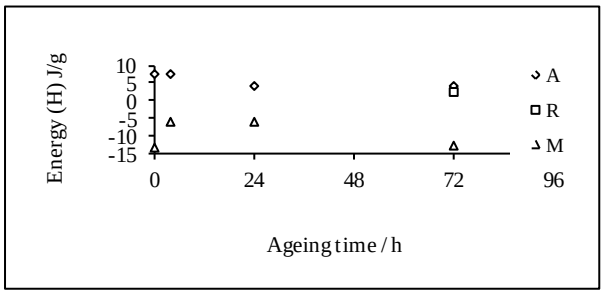

FIG. 8 - EFFECT OF ENTHALPY CHANGES OF THE ΔH_A, ΔH_R, AND ΔH_M WITH RESPECT TO THE AGEING TIME.

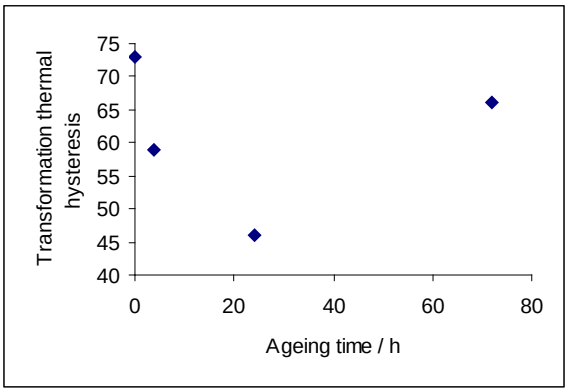

FIG. 9 - EFFECT OF AGEING TIME ON THE TRANSFORMATION THERMAL HYSTERESIS, H = A_F- M_S

Identifications of the Transformations

It is evident from the experimental results presented above that ageing under certain conditions may induce two-stage transformation behaviour in NiTi SMAs. The results presented in Figs.1-3 demonstrate that the single step transformation in heating and cooling relates to the B2↔B19′ phase transformations. Fig. 4 illustrates two-stage transformation behavior in both forward and reverses transformations, suggests that R-phase transformations occurred between the B2↔ B19′phases in aged for 72 h NiTi sample. The occurrences of the two separate B2↔R and R↔ B19′ transformations peaks signify that the two different free energy states of the R-phase with respect to the B19′ phase on heating, and B2 phase on cooling. In the context of aging, R is the R-phase formed around Ni_4Ti_3 precipitates formed in the affected NiTi matrix. This identification suggests the following experimental observations:

i. R-phase appeared comparatively, just below the $T^{B2\rightarrow B19'}$ phase, in the solutionized NiTi sample, and $T^{R\rightarrow B2}$ is compatible to the expected R-phase transformations.

ii. As shown in Fig. 4, temperature at which B2→ R merged in to R → B19′ on cooling at 51^{0}C, is compatible to the expected R-phase transformations in NiTi SMAs.

iii. R-phase appeared initially at temperatures well below the original B2→ B19′ transformations- this result is very peculiar for this aged temperature.

iv. The heat peak intensity, which is an indication of the transformation volume, of B2→ B19′, decreased continuously, whilst increases in ageing temperatures.

v. M_S decreased continuously in ageing treatment, from 70^{0}C (solutionized condition) to a low value of 51^{0}C aged for 72 hours.

Conclusions

Based on the above experimental investigations the following results were concluded:

- NiTi SMAs are very unstable even at this low temperature ageing treatment also.
- Stabilizations of the R-phase transformations occurred in aged for 72 hours sample on both heating and cooling also. The formations of the R-phase transformations depend upon the Ni_4Ti_3 precipitate segregates along the grain boundaries.
- Ageing of Ni-45.08 Wt%. Ti in the temperature range of 150^{0}C was effective in inducing R-phase transformations in NiTi SMAs and not only by the conventional ageing temperatures greater than or equal to 300^{0}C.
- The first transformations peak, on both heating and cooling, represents formation of the R-phase transformation. The formations of the single stage R-phase transformation behaviour is attributed to structural inhomogeneity of the matrix, both in terms of composition and of internal stress filed, caused by the formation of these precipitates.

- The critical transformation temperature required to the nucleation of the R-phase transformation is lower than the A_s temperature.
- The energy required to the nucleation of this phase $\Delta H_{B19' \rightarrow R}$ on heating cycle was 2.24 J/g, which was much lower than the reverse transformations (on cooling) $\Delta H_{B19' \rightarrow R} = -12.6$ J/g, this loss of about –8.55 J/g, is believed to be covered by the transformations between the two peaks of B19′→R and R→B2 in heating.
- The critical temperature for the nucleation of the martensite plates M_s temperature decreased continually with increasing ageing periods, it states that $T^{B19' \rightarrow B2}$, fluctuates in decreasing order. But there was not a large variation observed in M_f temperatures - M_f temperatures fluctuating between 41^0C and 51^0C.

ACKNOWLEDGEMENT

The corresponding author would like to express his sincere the staff at IIC (Instrument Instrumentation Center) at I.I.T. Roorkee, who helped him to carry out the DSC experiments, and express his sincere thanks to The U.S. Naval Air Systems Command who provided the NiTi shape memory Alloys.

REFERENCES

Miyazaki S, Otsuka K. Met. Trans. A 1986; 17A: 53–63.

K. Otsuka and K.Shinizu, M.Athlers Materials sciences and engg A, volume 273- 275, 15 Dec1999, Pages 595-599.

K. Hari Krishnan M.Tech dissertation report-2005, Metallurgical and Materials Engineering Department, I.I.T. Roorkee, Roorkee-247 667, India.

P.C. Su, S.K. Wu, Acta Materialia, 52 (2004) 1117-1122.

J.I. Kim, Yinong Liu, S. Miyazaki , Acta Materialia, 52 (2004) 487 –499.

International Journal of Material Science (IJMSCI) Volume 4 Issue 2, June 2014 www.ij-ms.org
doi: 10.14355/ijmsci.2014.0402.01

Carbon Nano-Tube and Nano-Fiber in Cement Mortar: Effect of Dosage Rate and Water-Cement Ratio

Nur Yazdani[1], Vinoth Mohanam[2]

[1]Civil Engineering, University of Texas at Arlington, Arlington, Texas 76019, U.S.A.

[2]Structural Engineer, Lloyd Engineering, Inc., Houston, Texas 77070, U.S.A.

[1]Yazdani@uta.edu; [2]Vinoth.Mohanam@mavs.uta.edu

Received 25 February, 2014; Revised 2 April, 2014; Accepted 5 May, 2014; Published 20 June, 2014

Abstract

Carbon nano-materials, especially Carbon Nanotubes (CNT) and Carbon Nanofibers (CNF), are two of the most prospective advanced materials for application in cement based products for the construction industry, due to their excellent material properties. In this study, their application in cement mortar was comparatively studied. Two mechanical properties, 28-day compressive strength and flexural strength, of CNT and CNF cement composites were investigated herein. The flow value of fresh mortar composites and Scanning Electron Microscope (SEM) images of hardened mortar samples were also explored. Composites with 0.1% and 0.2% of CNT and CNF and water/cement ratios of 0.35 to 0.5 were utilized, together with appropriate sonication techniques, based on the results from a previous study. Both CNT and CNF composites demonstrated significant increase in compressive strengths, as compared to plain mortar control samples (maximum 154% for CNT and 217% for CNF samples). The flexural strengths were also enhanced, although not at the same level as compressive strengths (maximum 53% for CNT and 50% for CNF samples). Water/cement ratios in the range of 0.35-0.4 were found to produce the higher strengths, together with a 0.1% dosage rate for the CNT/CNF. Statistical analysis of the test results showed the significance of the enhanced strengths. It seemed that the CNT was better dispersed in the cement matrix than the CNF, because a correlation between the flow test results and the compressive strengths was detected for the CNT samples. SEM (Scanning Electron Microscope) images showed fair to good dispersion of CNT/CNF in the hardened samples.

Keywords

Cement Mortar; Carbon Nanotubes; Carbon Nanofibers; Cementitious Products; Compressive Strength; Flexural Strength

Introduction

Cement products are premier materials in the construction industry. They have excellent compression properties but are weak in tension. To increase the tensile strength, these products can be reinforced with bars, rods, fibers or prestressing. Introduction of nanoparticles in cement based materials has gained popularity in recent years due to their excellent mechanical properties and application potential. Addition of carbon nanoparticles in the cementitious materials may provide extraordinary strength increase as well as controlling cracks.

Carbon Nanofibers (CNF) have an average diameter of 70 ~ 200 nanometers (nm) and an average length of 50 ~ 200 microns (ASTM 2011c), whereas Carbon Nanotubes (CNT) have an average diameter ranging from <1 nm up to 50 nm and an average length from 1 micron to 1 cm (ASTM 2011a). Introduction of CNF and CNT in cement based materials was not initially successful because of the high aspect ratios, causing dispersion problems of the CNF/CNT. Van der Waal's interaction tends to agglomerate them in bundles. Better dispersion could be achieved by ultrasonic agitation, and chemical treatment for sorting the fiber and treating with chemical solvents. Carbon nano-particles in cementitious compounds can be a very promising material (Jacobsen 2003).

The utilization of carbon fibers in the cement matrix started in the early 1990s, when Pu-Woei Chen and D.D.L. Chung introduced short carbon fibers in the cement mortar. An increase of 85% in flexural strength, 205% in flexural toughness and 22% in compressive

strength were obtained (Chen 1993). In 2000, Chung presented a review paper on cement-matrix structural composites for smart structures (Chung 2000). In 2004 the microstructure of the cement mortar with nanoparticles was displayed (Li 2004). The compressive strength and flexural strength of the cement mortar with nanoparticles were higher than plain cement paste. Another investigation of the dispersion of fibers in cement led to a major breakthrough in the usage of micro carbon fibers in the cement paste (Chung 2005). The dispersion of fibers was determined by measuring the electrical resistivity. Another study examined the abrasive resistance of concrete containing nanoparticles (Li 2006). The resistance improved significantly with the addition of nanoparticles and fibers. The compressive and flexural strengths improved when the nanoparticles and fiber content was 1% by weight of the cement. The flexural fatigue performance of concrete having nanoparticles was also investigated (Li 2007). Concrete containing 1% nanoTio2 by mass of cement had the best flexural fatigue strength. Another study performed testing on mechanical and electrical properties of self-consolidating concrete with CNF (Gao 2009). Concrete containing 1% CNF produced the best performance in terms of compressive strength and electrical resistivity.

In 2005, a paper was presented about the development in the production of CNT cement composite (Makar 2005). He suggested that the addition of single walled CNT in the cement composites accelerated the hydration process. CNT composites showed a classical reinforcing behavior of crack bridging and fiber pull-out mechanism, which was identified by SEM images. The wettability of multi walled CNT and the mechanical properties of the cement paste were investigated (Cwirzen et al 2009). It was determined that the tip sonication technique was most efficient in dispersion of the CNT. The bath sonication process was found to partly destroy the tube lengths. The research attained a 50% increase in the compressive strength in samples containing 0.045% polyacrylic acid polymer-treated CNT. The properties of both treated CNT (with sulphuric acid and nitric acid) and untreated CNT in cement composites were studied (Li 2007). SEM images revealed that the dispersion was uniform and bridging effect was observed. In 2009 the fracture characteristics and early strain capacity of CNT cement composites were investigated (Metaxa 2009). The results showed that the CNT of longer lengths in smaller quantities (0.025 – 0.048%) and shorter lengths in higher quantities (0.08%) could achieve good dispersions. Nano indentation results indicated that the CNT composites had higher stiffnesses and also were less porous. This reduction of pores led to significant effect on the early strain capacity of composites. A 2010 study examined issues like effect of ultrasonic energy, surfactant concentration and reinforcing effects on CNT dispersion (Konsta-Gdoutos 2009). The optimum ratio of surfactant to CNT was 4.0. A later study achieved an increment of 150% in the peak displacement in CNT-mortar, as compared to ordinary cement paste. (Yazdanbakhsh 2011)

In the study reported herein, a comparative analysis of the 28-day compressive strength, flexural strength and flow values of cement mortar reinforced with CNT and CNF was performed. The analysis demonstrated the relative performance of the two agents in cement mortar.

Materials and Methods

Ordinary Portland cement Type I/II with a compressive strength of 3500 psi (24 MPa), in accordance with ASTM standard C150, was used for the experiment. Graded sand having bulk density of 1497 kg/m^3 and specific gravity of 2.65 was used in accordance with ASTM standard C778. Glenium 7700, a high range water reducing admixture based on polycarboxylate ether was used as a surfactant as well as a dispersing agent. NC7000, a CNT from Nanocyl, produced by the Chemical Vapor Deposition (CVD) process, was used. PR-24-XT-LHT, a CNF from Pyrograf was also used. The properties of CNT and CNF are shown in Tables 1 and 2, respectively.

TABLE 1. PROPERTIES OF CNT – NC7000 (SOURCE: NANOCYL)

Property	Value
Average Diameter (nm)	9.5
Average Length (μm)	1.5
Carbon Purity, %	90
Metal Oxide, %	10
Surface Area, m2/g	250-300

TABLE 2. PROPERTIES OF CNF -PR-24-XT-LHT (SOURCE: PYROGRAF)

Fiber diameter, nm (average)	100
Fiber Length, μm (average)	50 - 200
CVD carbon overcoat present on fiber:	No
Surface area, m2/g:	43
Dispersive surface energy, mJ/m2:	155
Moisture, wt.%:	<5
Iron, ppm:	<14,000

Mixing Technique

The mixing technique for producing highly dispersed nanomaterial in cement mortar is crucial as it directly affects the mechanical properties of the cementitious composite. The dispersion of nanomaterial in the aqueous solution is very important before it is added to the cement mortar. A surfactant (plasticizer) was used in order to get a homogenous dispersion of CNT and CNF in water. Dosage rates for CNT and CNF were 0.1% and 0.2% by weight of the cement, respectively. A ratio of 0.008 for super plasticizer to cement was also selected. Water cement (w/c) ratios of 0.35, 0.40, 0.45 and 0.50 were employed herein. The CNT was sonicated for 30 minutes, while the CNF was sonicated for 15 minutes. These parameters were based on findings from a previous study (Manzur and Yazdani 2010). The CNT and CNF were dispersed in water with surfactant using a tip horn type sonicator. The tip used for the sonication was 0.5 inch (12 mm) in size and had a high intensity with an amplitude of 120μm. The sonication was done in 30 sec cycle interval to prevent overheating of the suspensions. Overheating may destroy the length of the nano particles; the length played a vital role in yielding the desired mechanical properties. The Sonicator setup is shown in Figure 1.

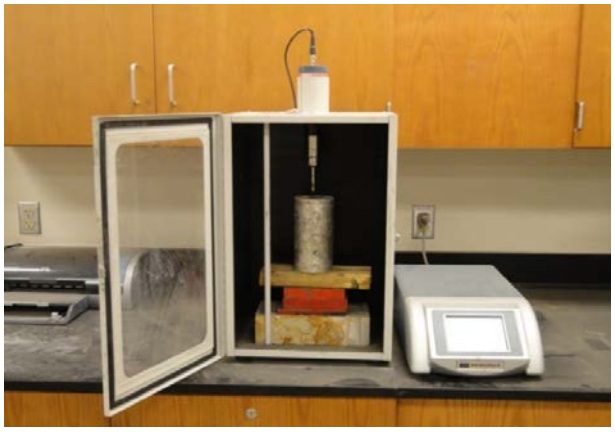

FIGURE 1. SONICATOR SETUP

Sample Preparation and Experiment Procedure

Compressive Strength

The ASTM C109 test procedure was used to determine the compressive strength of the cement mortar using 50 mm cubes (ASTM 2011c). The mortar consisted of 1 parts of cement and 2.75 parts of graded sand. A Hobart mixer with flat beater was used for the mixing of the mortar. After sonication, the nano particles were mixed with cement and sand for 4 min. After mixing, the mortar was placed in molds and demolded after 24 hr. and stored in a lime saturated water tank. The samples were loaded to failure in a universal testing machine at 7, 14 and 28 days of age (Figure 2). The loading rate was 890 to 1800 N/sec.

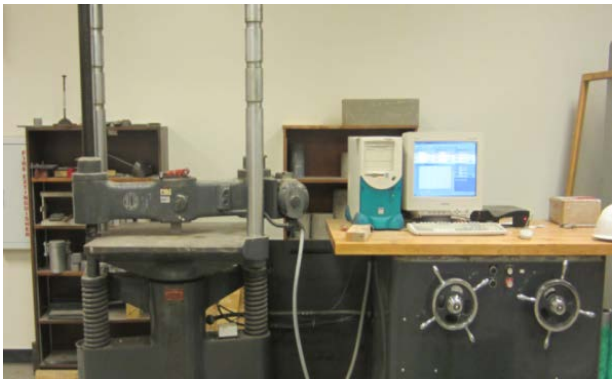

FIGURE 2: COMPRESSIVE STRENGTH TEST SET UP

Flexural Strength

The ASTM C348 test procedure was used to evaluate the flexural strength of the mortar using a sample size of 40 mm by 40 mm by 160 mm (Figure 3) (ASTM 2011a). The mixture proportion and the mixing procedures were identical to the compressive strength test. A three point loading set up was used with a loading rate of 2640 $\pm$ 110 N.

FIGURE 3: FLEXURAL STRENGTH TEST SET UP

Flow Test

The ASTM C1437 test procedure was used to calculate the flow of the mortar (ASTM 2011b). The mortar was placed 1 inch from bottom of the mold and compacted 20 times in 2 layers. The mortar was compacted and flushed with the surface of the mold. The flow mold was removed and the flow table was dropped 25 times in 15 seconds. The diameter of the mortar was recorded, and the percentage increase in the base diameter of the mortar was reported as the flow value (Figure 4).

FIGURE 4: FLOW OF MORTAR AFTER THE DROP

SEM Observations

The quality of dispersion of CNF and CNT in the cement matrix was explored using scanning electron microscope (SEM) images. The ZEISS Supra 55 VP, high performance variable pressure FE-SEM with patented GEMINI column technology, was used for this purpose. Broken mortar samples from the 28 day compressive strength testing was used for obtaining the SEM images.

Results and Discussion

CNT and CNF percentages of 0.1 % and 0.2% by weight of the cement were used in the cement composites to determine the compressive strengths at 28 day age. Four different w/c ratios were used. Compressive and flexural strengths of the composites were determined at 28 days. Comparative graphs of the compressive strength test results are presented in Figs. 5 and 6 for 0.1% and 0.2% dosage rates of the carbon additives, respectively. For control samples, the 0.4 w/c ratio yielded the maximum compressive strengths. Among the CNT samples, the maximum compressive strengths were demonstrated by samples with 0.45 – 0.5 w/c ratios for both concentrations (with strengths of around 38 - 45 MPa). Among the CNF samples, a lower w/c ratio of 0.40 produced superior strengths with both concentrations (52 - 54 MPa). Comparison of the CNT, CNF and control sample results at each w/c ratio in Figs. 5 and 6 clearly shows the higher strength achievements in the CNF samples at lower w/c ratios of 0.35 and 0.45 (Table 3). But the difficulty in having lower w/c ratio is the workability issue. Since CNFs have less surface area than CNT, it requires much less water content.

TABLE 3: PERCENTAGE INCREASE OF 28 DAY COMPRESSIVE STRENGTHS OVER CONTROL SAMPLES

	Dosage of CNT/CNF			
W/C Ratio	0.1% CNT	0.2% CNT	0.1% CNF	0.2% CNF
0.35	154	37	200	217
0.45	54	27	68	36

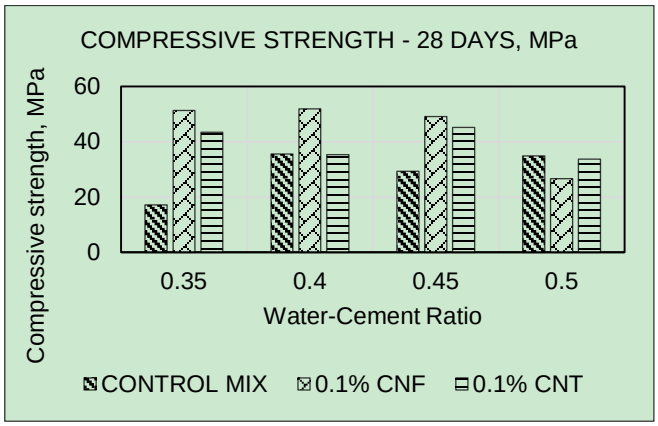

FIGURE 5: COMPRESSIVE STRENGTHS AT 28 DAYS, 0.1% CNT/CNF

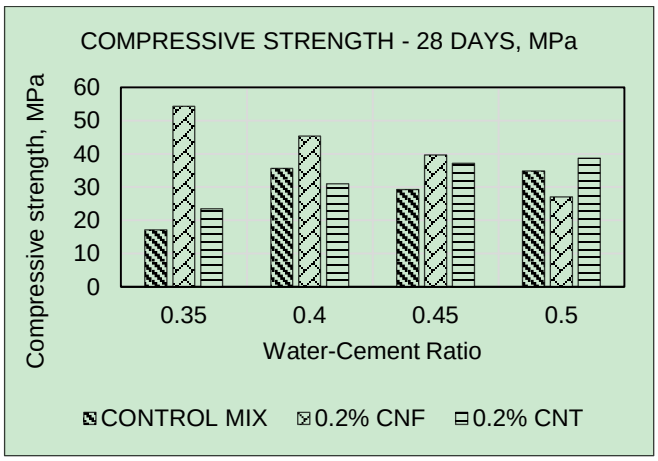

FIGURE 6: COMPRESSIVE STRENGTHS AT 28 DAYS , 0.2% CNT/CNF

The 28-day flexural strengths achieved by the 0.1% and 0.2% CNT/CNF samples are presented in Figures 7 and 8, respectively. Table 4 shows that the percentage flexural strength gains, as compared to the control samples, are impressive (27% - 53%) for 0.35 w/c ratio, although the gain is not as high as in the compressive strength samples. There is no clear indication of a particular combination of CNT/CNF and w/c ratio that resulted in better flexural strength production at 28 days. All nano reinforced samples performed better in flexural strength than the corresponding control samples. In general, the flexural strength outputs for

both CNT and CNF were greater at 0.35 w/c ratio than higher w/c ratios.

From both the test results it is obvious that irrespective of dosage rates of the CNT composites, w/c ratio of 0.45 enhanced the flexural strength of the CNT composites satisfying both strength and workability parameters.

Summarizing the compressive and the flexural test results, it is apparent that the best combination for compressive and flexural strength production, among the combinations explored herein, is CNF composites (0.1% - 0.2%) with 0.35% w/c ratio.

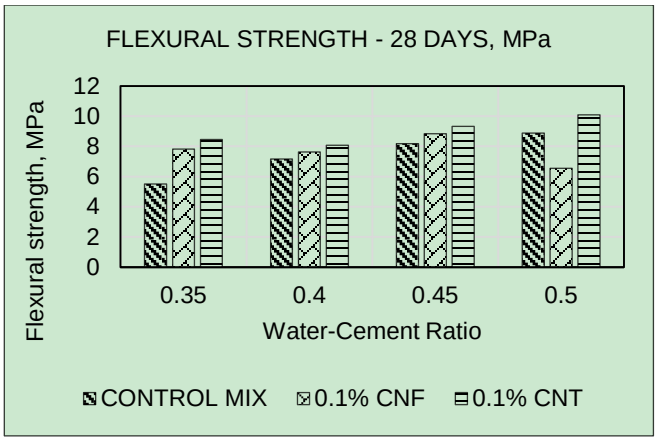

FIGURE 7: FLEXURAL STRENGTHS AT 28 DAYS, 0.1% CNT/CNF

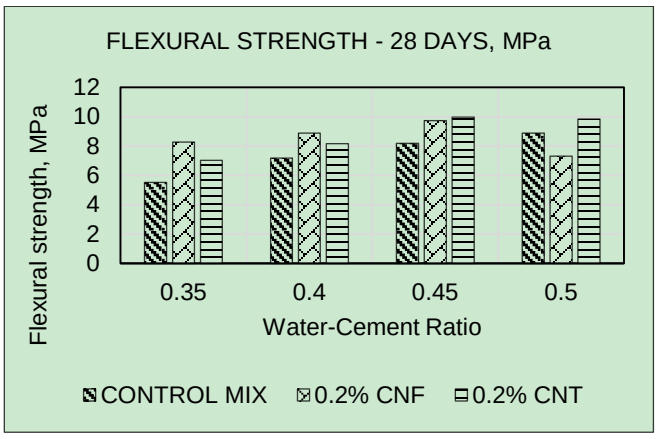

FIGURE 8: FLEXURAL STRENGTHS AT 28 DAYS, 0.2% CNT/CNF

TABLE 4: PERCENTAGE INCREASE OF FLEXURAL STRENGTHS OVER CONTROL SAMPLES

	Dosage of CNT/CNF			
W/C Ratio	0.1% CNT	0.2% CNT	0.1% CNF	0.2% CNF
0.35	53	27	42	50
0.45	14	22	8	19

Statistical Analysis

Statistical analysis was performed to determine if the nano-composites achieved significantly greater strengths than the control samples. The t-test was adopted for this purpose. This test is one of the powerful tools in manipulating the mean of a normally distributed population where the sample size is small and the standard deviation is unknown. The t-test was performed to see if the differences in the mean of each sample set were statistically different. P-value method was used for determining the hypothesis testing. The null hypothesis can be rejected if the P-value is less than the significance level of 0.05. This would signify that the composite strength was significantly greater than the control sample strength. The test results for compressive and flexural strengths are presented in Tables 5 and 6, respectively.

TABLE 5: T-TEST RESULTS OF 28-DAY COMPRESSIVE STRENGTHS

Mix Proportion	Control samples, MPa (ksi)	Composite samples, MPa (ksi)	P<0.05?
0.1% CNF + 0.35 w/c	17.13	51.30	**Yes**
0.1% CNF + 0.40 W/C + 0.008 SP	35.63	51.92	**YES**
0.1% CNF + 0.45 W/C + 0.008 SP	29.27	49.13	**YES**
0.1% CNF + 0.50 W/C + 0.008 SP	35.06	26.61	**YES**
0.2% CNF + 0.35 W/C + 0.008 SP	17.13	54.32	**YES**
0.2% CNF + 0.40 W/C + 0.008 SP	35.63	45.36	**YES**
0.2% CNF + 0.45 W/C + 0.008 SP	29.27	39.69	**YES**
0.2% CNF + 0.50 W/C + 0.008 SP	35.06	27.11	**YES**
0.1% CNT + 0.35 W/C + 0.008 SP	17.13	43.44	**YES**
0.1% CNT + 0.40 W/C + 0.008 SP	35.63	35.30	NO
0.1% CNT + 0.45 W/C + 0.008 SP	29.27	45.22	**YES**
0.1% CNT + 0.50 W/C + 0.008 SP	35.06	33.73	NO
0.2% CNT + 0.35 W/C + 0.008 SP	17.13	23.46	**YES**
0.2% CNT + 0.40 W/C + 0.008 SP	35.63	30.96	NO
0.2% CNT + 0.45 W/C + 0.008 SP	29.27	37.13	**YES**
0.2% CNT + 0.50 W/C + 0.008 SP	35.06	38.76	NO

From Table 5, it is clearly evident that all CNF composites gained significant compressive strengths over the control samples. For CNT composites, the compressive strengths were significantly different at 0.35 w/c ratio.

Table 6 shows that the flexural strengths of CNT and

CNF composites produced mixed results. Flexural strengths did not show a clear trend of significant increase over the control sample strengths, as opposed to the compressive strength cases.

Significance of Flow Value

The flow value an indicator of the workability and ease of placement of cement mortars. Relationship

TABLE 6: T-TEST RESULTS OF 28-DAY FLEXURAL STRENGTHS

MIX PROPORTION	Control samples, MPa (ksi)	Composites, MPa (ksi)	P<0.05?
0.1% CNF + 0.35 w/c	5.51	7.82	Yes
0.1% CNF + 0.40 W/C + 0.008 SP	7.17	7.63	No
0.1% CNF + 0.45 W/C + 0.008 SP	8.18	8.84	NO
0.1% CNF + 0.50 W/C + 0.008 SP	8.88	6.54	NO
0.2% CNF + 0.35 W/C + 0.008 SP	5.51	8.27	YES
0.2% CNF + 0.40 W/C + 0.008 SP	7.17	8.87	YES
0.2% CNF + 0.45 W/C + 0.008 SP	8.18	9.72	NO
0.2% CNF + 0.50 W/C + 0.008 SP	8.88	7.30	NO
0.1% CNT + 0.35 W/C + 0.008 SP	5.51	8.46	YES
0.1% CNT + 0.40 W/C + 0.008 SP	7.17	8.08	NO
0.1% CNT + 0.45 W/C + 0.008 SP	8.18	9.33	NO
0.1% CNT + 0.50 W/C + 0.008 SP	8.88	10.08	YES
0.2% CNT + 0.35 W/C + 0.008 SP	5.51	7.02	NO
0.2% CNT + 0.40 W/C + 0.008 SP	7.17	8.16	NO
0.2% CNT + 0.45 W/C + 0.008 SP	8.18	9.97	NO
0.2% CNT + 0.50 W/C + 0.008 SP	8.88	9.83	NO

between the flow values and the compressive strength of CNT and CNF composites are shown in Figures 9 and 10 with corresponding trend lines. The compressive strength of CNT cement composites increased when the flow value was higher, especially at the 0.2% mixing ratio. This phenomenon indicated that the CNT was well dispersed in the cement matrix. CNT-mortar mixes with high compressive strengths would be easier to work with in the field. The compressive strength of CNF composites decreased in general with increasing flow values for both 0.1% and 0.2% mixing ratios. This pattern indicated that the CNF-mortar with higher compressive strengths would be relatively more difficult to work with in the field.

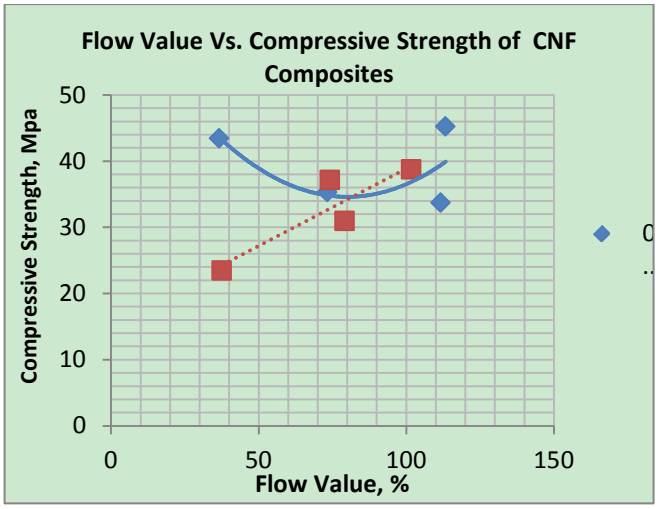

FIGURE 9: FLOW VALUE VS. COMPRESSIVE STRENGTH OF 0.1% AND 0.2% CNT COMPOSITES AT 28 DAYS

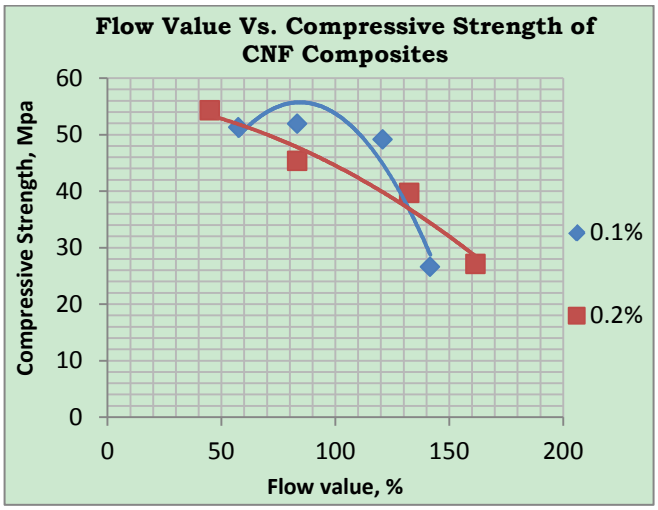

FIGURE 10: FLOW VALUE VS. COMPRESSIVE STRENGTH OF 0.1% AND 0.2% CNF COMPOSITES AT 28 DAY

SEM Imaging Results

From the sample SEM images of hardened CNF and CNT composites in Figure 11 , it is observed that the CNF and CNT were reasonably evenly dispersed in the mortar matrices. Although CNF and CNT exhibited visually uniform looking dispersion in the aqueous medium after sonication, the dispersion was not fully achieved when mixed with the cement. Re-agglomeration of CNF and CNT in the cement matrices took place due to absorption of water by the cement. Additional sonication is, therefore, necessary to achieve proper dispersion of CNT and CNF in the cement matrix.

The following conclusions may be made based on the

study reported herein:

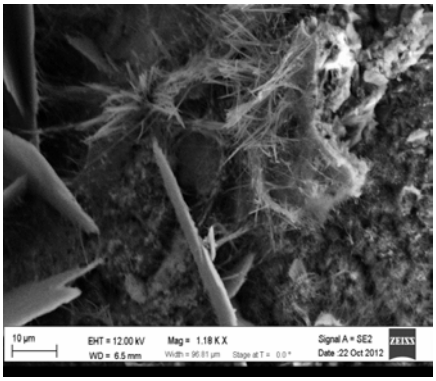

(a) 0.1% CNF, 0.40 w/c

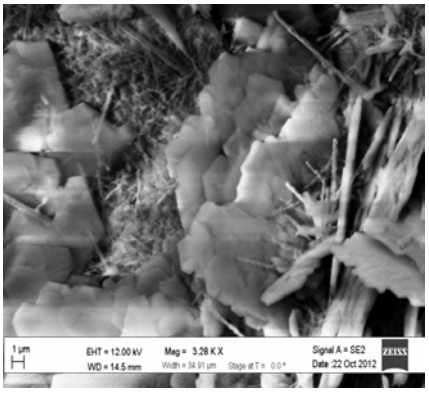

(b) 0.2% CNF, 0.40w/c

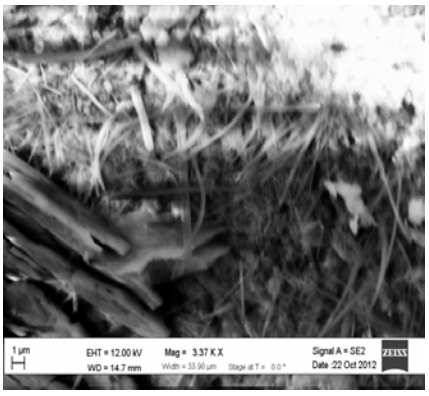

(c) 0.1% CNF, 0.45 w/c

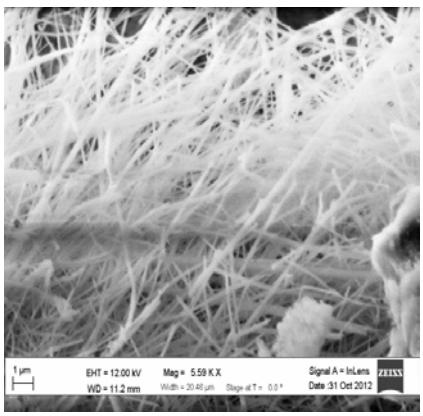

(D) 0.2% CNF, 0.45 W/C

FIGURE 11: SEM IMAGES OF HARDENED SAMPLES

[1] The major difficulty in using the nanoparticles within the cement matrices was the rate of dispersion. The nanoparticles attracted each other forming either bundles or ropes due to van der Waal's force. Therefore ultrasonication, a method used to disperse the nanoparticles in the aqueous medium, was pursued.

[2] An effective w/c ratio of 0.45, which produced higher compressive and flexural strengths, was obtained. CNT percentage of 0.1 cement composites attained 54% and 14% higher compressive and flexural strength than plain cement mortar. Similarly, 0.1% CNF cement composites achieved 67% and 8% higher compressive and flexural strengths, compared to plain cement mortar. These results indicated that the CNF and CNT cement composites are promising material for the reinforcement of cement mortar.

[3] The degree of dispersion was verified using SEM images. SEM images of CNT and CNF cement composites showed a few bundles and clumps of CNF and CNT in the cement matrix. Poor dispersion may be due to re-agglomeration of CNF and CNT by absorption of water from the cement, when mixed to form the cement mortar.

[4] The primary results from the compressive and flexural strength were promising in spite of some poor dispersion observed in the hardened cement mortar.

[5] The compressive strength of CNT composites increased when the flow value was higher, especially at the 0.2% mixing ratio. CNT-mortar mixes with high compressive strengths would be easier to work with in the field. The compressive strength of CNF composites decreased in general with increasing flow values for both 0.1% and 0.2% mixing ratios. This pattern indicated that the CNF-mortar with higher compressive strengths would have relatively less workability than the CNT mortars.

[6] Both CNT and CNF are promising reinforcing materials for cementitious products. Significant additional work is needed on adequate dispersion, bonding evaluation, strength and durability evaluation to completely validate the composite products.

REFERENCE: -

American Society for Standard Testing and Materials (ASTM), (2011a), "Standard Test Method for Flexural Strength of Hydraulic-Cement Mortars." ASTM C348-08.

American Society for Standard Testing and Materials (ASTM), (2011b). Standard Test Method for Flow of Hydraulic Cement Mortar. ASTM C 1437-07.

American Society for Testing and Materials (ASTM), (2011c), Standard Test Method for Compressive Strength of Hydraulic-Cement Mortars. ASTM C 109-11b.

Chen, P. W., and Chung, D. D. L. (1993). Concrete reinforced with up to 0.2% volume of short carbon fibres. Composites, 24(1), 33-52.

Chung, D. D. (2005). Dispersion of short fibers in cement. Journal of materials in civil engineering, 17(4), 379-383.

Chung, D. D. L. (2000). Cement-matrix composites for smart structures. Smart materials and structures, 9(4), 389.

Cwirzen, A., Habermehl-Cwirzen, K., Nasibulina, L. I., Shandakov, S. D., Nasibulin, A. G., Kauppinen, E. I., Mudimela, and Penttala, V. (2009). CHH Cement Composites, Nanotechnology in Construction 3, pp. 181-185.

Gao, D., Sturm, M., and Mo, Y. L. (2009). Electrical resistance of carbon nanofiber concrete. Smart Materials and Structures, 18(9), 095039.

Jacobsen, R. L., Walters, K. R., Glasgow, D. G., & Wang, C. S. (2003, October). Carbon Nanofiber Filled Materials for Charge Dissipation. In 8 th Spacecraft Charging Technology Conference.

Konsta-Gdoutos, M. S., Metaxa, Z. S., and Shah, S. P. (2010). Multi-scale mechanical and fracture characteristics and early-age strain capacity of high performance carbon nanotube/cement nanocomposites. Cement and Concrete Composites, 32(2), 110-115.

Li, H., Xiao, H. G., Yuan, J., and Ou, J. (2004). Microstructure of cement mortar with nano-particles. Composites Part B: Engineering, 35(2), 185-189.

Li, H., Zhang, M. H., and Ou, J. P. (2006). Abrasion resistance of concrete containing nano-particles for pavement. Wear, 260(11), 1262-1266.

Li, H., Zhang, M. H., and Ou, J. P. (2007). Flexural fatigue performance of concrete containing nano-particles for pavement. International Journal of Fatigue, 29(7), 1292-1301.

Makar, J. M. and Beaudoin, J. J. (2004). Carbon nanotubes and their application in the construction industry. SPECIAL PUBLICATION-ROYAL SOCIETY OF CHEMISTRY, 292, 331-342.

Manzur, T. and Yazdani, N. (2010). Strength Enhancement of Cement Mortar with Carbon Nanotubes: Early Results and Potential. Journal of the Transportation Research Records, No. 2142, pp. 102-108.

Metaxa, Z. S., Konsta-Gdoutos, M. S., and Shah, S. P. (2009). Carbon nanotubes reinforced concrete. Nanotechnology of Concrete: The Next Big Thing is small, 11-20.

Yazdanbakhsh, A., Grasley, Z. C., Tyson, B., and Al-Rub, R. A. (2009). Carbon nano filaments in cementitious materials: some issues on dispersion and interfacial bond. Proceedings of the American Concrete Institute (ACI'09), 267, 21-34.

International Journal of Material Science (IJMSCI) Volume 4 Issue 2, June 2014 www.ij-ms.org
doi: 10.14355/ijmsci.2014.0402.02

Microencapsulation of Ascorbic Acid as Redox Initiator with Tripalmitin

Yoshinari Taguchi[1], Masato Tanaka[2*]

[1,2]Graduate School of Science and Technology, Niigata University, 8050, Ikarashi 2-nocho, Niigata-shi, Niigata 950-2181, Japan

[*]tanaka@eng.niigata-u.ac.jp

Received 24 September, 2013; Revised 27 January, 2014; Accepted 20 February, 2014; Published 20 June, 2014

Abstract

We have tried to microencapsulate powdery ascorbic acid as a redox initiator for polymerization with tripalmitin of the shell material by the coating method in order to give the core water resisting qualities. Microencapsulation was performed in the mill pot in which the core and the shell were mixed together with the pulverizing solvent.

In the experiment, the added amount of tripalmitin as the shell material and the concentration of ethyl alcohol as the pulverizing solvent were mainly changed stepwise. It was investigated how the operational conditions affected the characteristics of microcapsules such as the water proof degree, the content of core material, the microencapsulation efficiency and the yield.

The water proof degree of microcapsules was increased with the added amount of shell material and the concentration of pulverizing solvent. The microencapsulation efficiency was changed from 70 to 90% according to the operational conditions. The yield and the content were changed from 90 to 100% and from 35 to 46% according to the operational conditions, respectively. It was found that the microcapsules were able to induce polymerization of methyl methacryate by breaking the microcapsule shell due to heating.

Keywords

Microencapsulation; Dry Coating Method; Ascorbic Acid; Tripalmitin; Redox Initiator

Introduction

Many kinds of microcapsules have been prepared to apply to the various fields such as information recording materials, paintings, cosmetics, food materials, adhesives, medicine and so on (Kondo, 1967; Tanaka, 2008).The main purposes of microencapsulation are to protect the core material from environment, to release the core material according to occasion demands, to handle the gaseous and the liquid core materials as the solid particles (Tanaka, 2008). Moreover, we can prepare the microcapsules with the various functions by how to select the physical properties of the core and the shell materials and how to combine these materials. For examples, there are the combination of the hydrophilic core materials with the hydrophobic and/or the hydrophilic shell materials, and the combination of the inorganic core materials with the organic and/or the inorganic shell materials. Also, we can select the shell materials with the various physical properties such as magnetism, electric conductivity, thermal conductivity, chemical resistance, biodegradability and so on (Tanaka & Hayashi, 1989; Tanaka & Hayashi, 1990; Tanaka, et al., 1992; Tanaka, et al., 1992; Kimura, et al., 1995; Taguchi, et al., 1999; Taguchi, et al., 2001; Taguchi, et al., 2003).

Ascorbic acid is well known as a redox initiator for polymerization of styrene and methyl methacrylate. If the redox initiator could be microencapsulated and added into these monomers beforehand, polymerization may be induced by breaking the microcapsules due to appropriate stimuli. In dental treatment using polymerization stated above, it has been strongly desired to microencapsulate powdery ascorbic acid with the hydrophobic material. Namely, if ascorbic acid as a redox initiator for polymerization could be microencapsulated with the hydrophobic and chemical resistance materials, the microcapsules could be added into monomer such as styrene and methyl methacrylate beforehand and polymerization should be induced by breaking microcapsules due to heating. As a result, it may be expected that dental treatment has to be extremely improved.

In general, it is well known that the preparation method by using the water phase is not suitable to microencapsulation of water soluble core material (Kofuji, et al., 2005; Chen, et al., 2013; Luizildo, et al., 2013; Michael, et al., 2011, 2012). For an example, as the water soluble core materials dissolve in the water phase in the microencapsulation process, the content of core materials may be decreased. Accordingly, it is desirable that the preparation method without the water phase is applied for microencapsulation of the water soluble materials and the hydrophilic materials. So, it is necessary to develop the method without any water for preparing the microcapsules containing the water soluble materials or the hydrophilic materials.

In this study, it is tried to microencapsulate powdery ascorbic acid with tripalmitin as the hydrophobic and thermal responsible shell material by using the dry coating method, in which the core and the shell materials are mixed in the mill pot together with pulverizing solvent and the surface of core material is coated with the shell material.

The purposes of this study are to establish the preparation method of microcapsules containing the water soluble ascorbic acid, to investigate how the operational conditions such as the added amount of shell material and the concentration of ethyl alcohol of pulverizing solvent affect the characteristics of microcapsules and to apply the microcapsule to polymerization of methyl methacrylate.

Experimental

Materials

Water soluble core material was L-(+)-ascorbic acid (LAA) with the mean diameter of 20 μm (Wako Pure Chemical Industries, Ltd.). Tripalmitin (TP) with the melting point of 80℃ was meth used as the hydrophobic shell material, which was purchased from Kanto Chemical Co., Inc. Ethyl alcohol (EtOH) (Kanto Chemical Co., Inc.) was used as the pulverizing solvent for the shell material. Methyl methacrylate monomer (Kanto Chemical Co., Inc.) was used to investigate whether the microcapsules are able to induce polymerization or not.

Preparation of Microcapsules

Fig. 1 shows the purpose of microencapsulation and the microencapsulation mechanism.

In general, it is well known that the naked active materials are easily deactivated by oxygen or humidity. If the active materials are microencapsulated by the shell materials with the barrier ability to oxygen or humidity, the activity of core materials has to be kept for long time. In microencapsulation of the core materials deactivated easily by oxygen or humidity, it is necessary to develop the microencapsulation method without air and humidity. Taking these things into consideration, we have adopted the dry coating method which is performed under nitrogen atmosphere using only the pulverizing solvent.

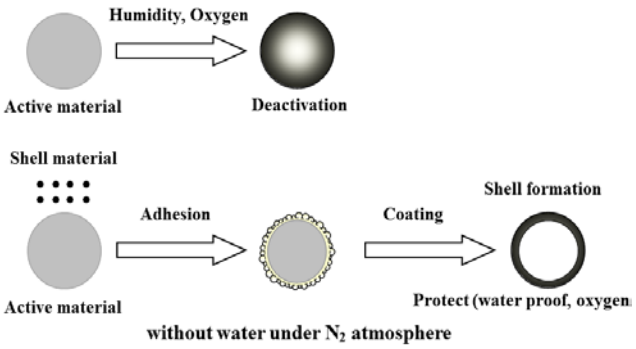

FIG. 1 PURPOSE OF MICROENCAPSULATION AND MICROENCAPSULATION MECHANISM

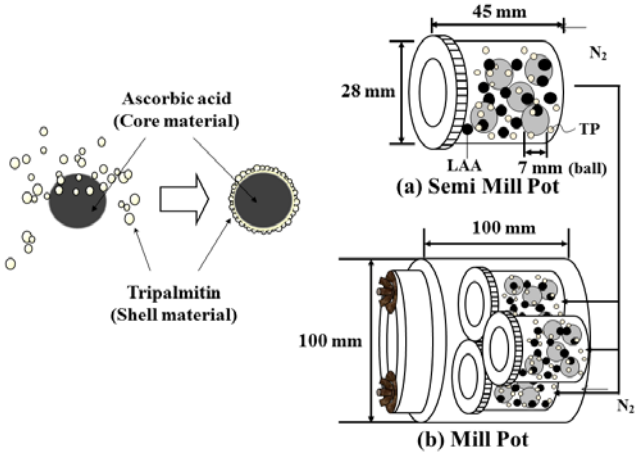

FIG. 2 SCHEMATIC DIAGRAM OF EXPERIMENTAL APPARATUS FOR PREPARING MICROCAPSULES

Figs. 2 and 3 show the schematic diagram of experimental apparatus and the flow chart for preparing the microcapsules, respectively.

First, in order to make sure of the shell formation, LAA and TP were premixed for ten min at the revolution speed of 60 rpm in the semi mill pot as shown in Fig. 1a by adding the given volume of EtOH. In the semi mill pot, ten nylon balls with the diameter of 7 mm were added. Then, the semi mill pot containing the mixture of LAA and TP was set in the mill pot as shown in Fig. 1b and mixed for 6 h at the

revolution speed of 60 rpm. In the mill pot, the three semi mill pots were set to increase the production amount of microcapsules. Microencapsulation may progress in turn such as partial solution of TP with EtOH, adhesion of TP and film formation on the surface of LAA powder. In the preparation method of microcapsules presented here, the concentration of EtOH (C_E: wt% to TP) and the added amount of TP to change the feed ratio (R) of TP to LAA were mainly changed. Table 1 shows the experimental conditions adopted in this study.

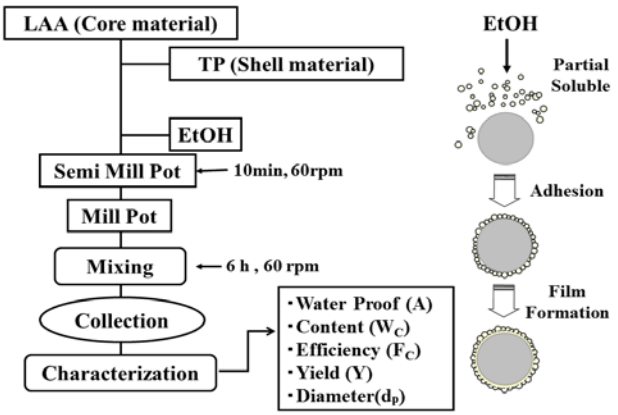

FIG. 3 FLOW CHART FOR PREPARING MICROCAPSULES

TABLE 1 EXPERIMENTAL CONDITIONS

L-(+)- Ascorbic acid (d_p= 20μm)	2.5g
Tripalmitin (d_p= 21.5μm)	1.1～3.0g
Feed ratio of TP to LAA	R=7/3, 6/4, 5/5, 4/6, 3/7
Pulverizing Medium	Ten nylon balls (1.55g)
Premixing Time (Semi mill pot)	10min
Rotational velocity (Semi mill pot)	60rpm
Mixing Time	6h
Rotational velocity	60rpm
Concentration of EtOH(C_E)	0wt%, 0.629wt%, 1.26wt%, 1.89wt%

Characterization of Microcapsules

Microcapsules prepared thus were characterized about the following things:

1) Observation of Microcapsules

The surface and morphology of a microcapsule were observed by scanning electron microscope (SEM) (VE-9800, Keyence Corp., Osaka, Japan).

2) Mean Diameter of Microcapsules

The diameters (d_{Pi}) of about 200 (n) microcapsules were directly measured from SEM photographs of them. From these diameters, the mean Sauter diameter (d_P) was calculated by the following equation.

$$d_P = \frac{\sum n_i \, d_{pi}^3}{\sum n_i \, d_{pi}^2} \quad (1)$$

3) Water Proof Degree

LAA of given weight was dissolved into distilled water of 40 cm^3 and then, the concentration of NaOH to neutralize the LAA aqueous solution was measured by titrating with 0.02mol/L NaOH aqueous solution. From these results, the correlating curve between the concentration of LAA and that of NaOH was obtained beforehand. Then, the microcapsules of 0.5 g were added into distilled water of 40 cm^3 to be dispersed for 30 min by mixing gently with the magnetic stirrer, under which conditions any microcapsules were not broken mechanically. After this operation, the given volume (10 cm^3) of aqueous solution, in which the microcapsules were dispersed, was sampled out and then, the concentration of NaOH to neutralize this solution was measured. By comparing the measured concentration of NaOH with the correlating curve, the concentration of LAA leaking from the microcapsules was estimated. Moreover, the remaining microcapsules were redispersed in distilled water of 40 cm^3 and broken by heating up to 80℃ (> melting point of TP) to completely dissolve LAA microencapsulated. Thus, the weight of LAA not leaking from the microcapsules was estimated in the same manner as these stated above. From these values, the water proof degree (A) was calculated by using the following equation.

$$A = \frac{\text{weight of LAA remaining in microcapsules}}{\text{initial weight of LAA in microcapsules}} \quad (2)$$

4) Content, Microencapsulation Efficiency, Yield

The content (W_C) of core material, the microencapsulation efficiency (F_C), the yield (Y) were calculated by using the following equations from the measured values.

$$W_C = \frac{\text{total weight of LAA microencapsulatd}}{\text{weight of microcapsules}} \quad (3)$$

$$F_C = \frac{\text{total weight of LAA microencapsulated}}{\text{weight of LAA in feed}} \quad (4)$$

$$Y = \frac{\text{weight of microcapsules}}{\text{weight of TP and LAA in feed}} \quad (5)$$

5) Application of Microcapsules to Polymerization of MMA

The microcapsules (0.5 g) were added into a beaker, in which 10cm^3 of MMA monomer dissolving potassium persulfate (KPS) was poured beforehand. It was observed whether polymerization was induced by heating the beaker at 130℃ and breaking the microcapsules or not. For comparison, the same experiments as stated just above were conducted by adding only LAA with heating at 50℃ and by adding the microcapsules with heating at 50℃, respectively. The microcapsules were not broken at 50℃.

Results and Discussion

Fig. 4 shows the SEM photographs of LAA powder (Fig. 4a) and microcapsule (Fig. 4b) which was prepared under the conditions of R = 5/5 and C_E = 1.26 wt%. From these photographs, it is found that LAA is irregular granule with the mean diameter of ca.20 μm and is coated well with TP.

Furthermore, a few LAA granules are agglomerated each other at the microencapsulation process to form larger microcapsules.

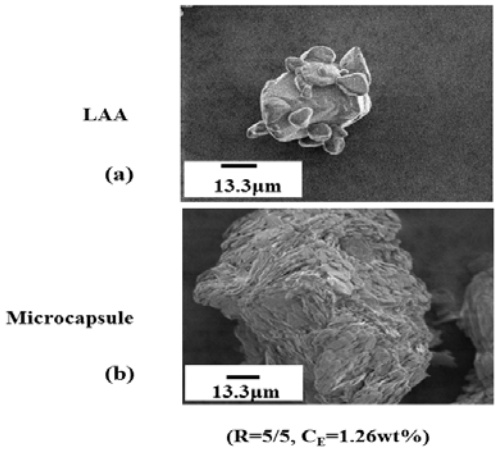

FIG. 4 SEM PHOTOGRAPHS OF LAA AND MICROCAPSULE

Fig. 5 shows the effect of feed ratio (R) of TP to LAA on the microencapsulation efficiency (F_C), the content (W_C) of core material, the water proof degree (A), the yield of microcapsules (Y) and the mean diameter (d_P). From this figure, the following interesting results are obtained. The yield of microcapsules is almost above 96% and the microencapsulation efficiency above 82% can be obtained. From these results, the microencapsulation process is found to progress satisfactory. However, on changing the feed ratio from 7/3 to 3/7, the water proof degree is decreased from 100% to 45% and the content of core material is increased from 30% to 65%. It is considered that the water proof degree may decrease by decrease in the shell thickness. The shell thickness is able to be estimated to decrease to ca.28% of the shell thickness (Ca. 9.3 μm) at R=7/3. In this estimation, it is supposed that LAA is spherical and all TP added is adhered on the surface of LAA. The contents of core material measured are smaller than those (40 to 70) calculated on the basis of the feed ratio. This may be considered to be due to adhesion of the shell and the core materials on the mill pot wall or the pulverizing medium. The mean diameter of microcapsules is ca. 42 μm at R=7/3 and increased with R, but becomes the constant value of ca. 62 μm at R=5/5, 4/6 and 3/7.

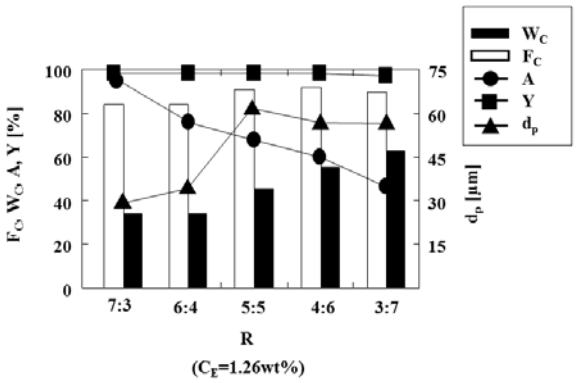

FIG. 5 EFFECT OF FEED RATIO ON CHARACTERISTICS OF MICROCAPSULES

Fig. 6 shows the SEM photographs of microcapsules prepared by changing R. The shell of microcapsule at R=7/3 is found to be denser (closely packed) and thicker than that at R=3/7 because of more TP. The characteristics of microcapsules are strongly affected by the concentration of pulverizing solvent, because adhesion and shell formation of TP are affected by pulverizing solvent.

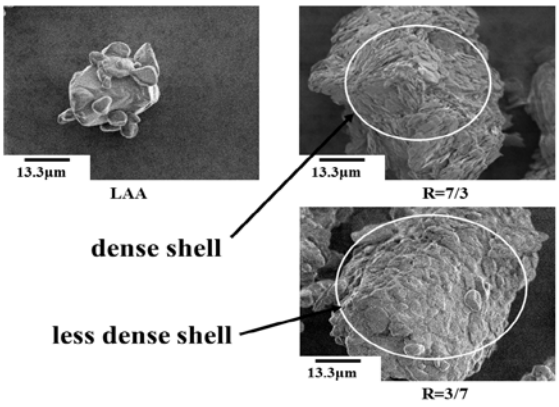

FIG. 6 SEM PHOTOGRAPHS OF MICROCAPSULES PREPARED BY CHANGING R

Fig. 7 shows the dependencies of the microencapsulation efficiency (F_C), the content of core material (W_C), water proof degree (A), the yield (Y) and the mean diameter (d_P) on the concentration of EtOH. From this figure, the following results are

obtained. The content of core material is almost kept constant (W_C = 40%) over the region of the concentration of EtOH from 0 to 0.63 wt% and then, slightly decreases with the concentration of EtOH. The mean diameters of microcapsules decrease from 200 μm to 120 μm with the concentration of EtOH. The microencapsulation efficiency decreases from 80% to 65 % with the concentration of EtOH. The water proof degree increases from 50% (C_E = 0) to 75% (C_E = 1.26 wt%) and then, decreases at C_E = 1.89 wt%. The yield slightly decreases from 100 to 90% with the concentration of EtOH.

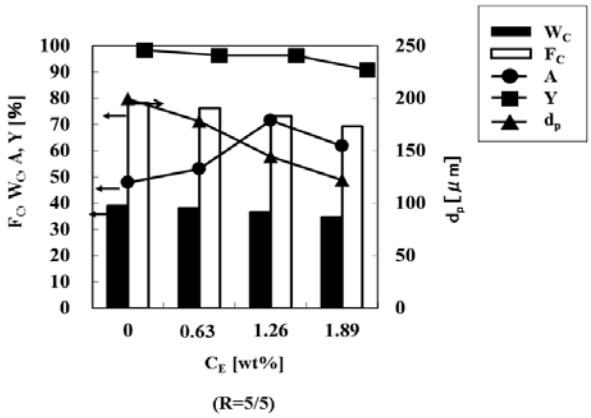

FIG. 7 EFFECT OF CONCENTRATION OF ETOH ON CHARACTERISTICS OF MICROCAPSULES

From these results, the following microencapsulation mechanism may be presented as shown in Fig. 8 At the lower concentration of EtOH, TP may partially dissolve and adhere on the part of the surface of LAA. In this case, the dense shell may not be formed. On increasing the concentration of EtOH, the more the partial soluble TP becomes, the more the adhered TP becomes. As a result, the complete dense shell may be formed. According to this phenomena, the water proof degree has to be increased. However, at the higher concentration of EtOH, a portion of the complete shell formed already may be re-dissolved and removed from the surface of LAA. Furthermore, a portion of microcapsules may adhere on the mill pot wall. Accordingly, the yield at C_E = 1.89 wt% may become smaller than that at R = 5/5 and C_E = 1.26 wt% in Fig. 5 and the content and the microencapsulation efficiency have to be decreased.

Fig. 9 shows the SEM photographs of microcapsules prepared by changing the concentration of EtOH. It is found that the shell becomes denser by adding EtOH.

Fig. 10 shows the result of application of microcapsules to polymerization of methyl methacrylate. In the case of addition of only LAA into MMA monomer at 50℃, polymerization is induced and polymethyl methacrylate is formed at elapsing time of 15 min. In the case of addition of microcapsules at 50℃, polymerization is found to be not induced even at elapsing time of 15 min. On the other hand, in the case of addition of microcapsules at 130℃, it is found that polymerization is induced and polymethyl acrylate is formed at elapsing time of 15 min. From these results, LAA of core material is microencapsulated well with TP and the microcapsules with responsibility to temperature of 80℃ are able to be prepared.

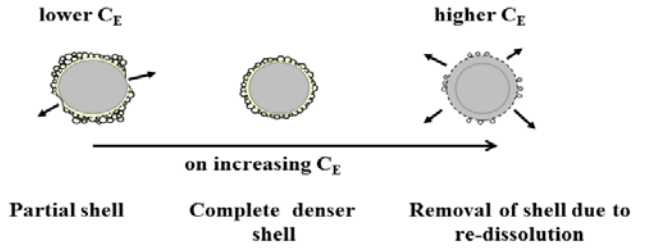

FIG. 8 MECHANISM OF MICROENCAPSULATION

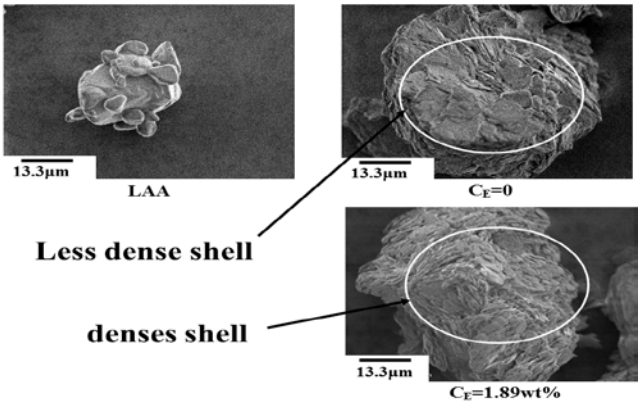

FIG. 9 SEM PHOTOGRAPHS OF MICROCAPSULES PREPARED BY CHANGING CONCENTRATION OF ETOH

FIG. 10 APPLICATION OF MICROCAPSULES TO POLYMERIZATION

Conclusion

We have tried to microencapsulate ascorbic acid with

tripalmitin to give the microcapsules both the water proof and the thermal responsibility and to apply the microcapsules to polymerization of methyl methacrylate.

The following results were obtained.

1. The water proof was able to be increased by increasing the added amount of shell material and the concentration of EtOH, but decreased by the excess concentration of EtOH.

2. The yield, the microencapsulation efficiency and the content of core material were decreased with the concentration of EtOH.

3. The water proof degree of ca. 100% can be obtained at C_E = 1.26 wt% and R = 7/3.

4. Polymerization of methyl methacrylate can be induced by breaking the microcapsules with heating.

REFERENCES

Isao Kimura, Haruyuki Yoshii, Natsukaze Saito, Masato Tanaka, "Preparation of composite particles constituted of fine aluminum nitride powder and polystyrene by suspension polymerization," Journal of the Society of Powder Technology Japan 32, (1995): 229-236.

Kyoko Kofuji, Chun-Jun Qian, etals, "Preparation of chitosan microparticles by water-in-vegetable oil emulsion coalescence technique," Reactive & Functional Polymers 62, (2005): 77-83.

Luizildo Pitol-Filho, Vanja Kokol, Bojana Voncica, "Synthesis and Characterization of Ethyl Cellulose Microcapsules Containing Model Active Ingredients," Macromolecular Symposia 328, (2013): 45-55.

Masato Tanaka, "Key point of preparation of nano/microcapsules," Techno system Publishing Co. Ltd., Tokyo, Japan, 2008.

Masato Tanaka, Atsushi Saito, Kazuhiko Hosogai, Isao Kimura, "Preparation of Fine Polymer Particles Coated Uniformly with Magnetite Powder by Suspension Polymerization," Kagaku Kogaku Ronbunshu 18, no. 3 (1992): 330-337.

Masato Tanaka, Kazuhiko Hosogai, "Suspension Polymerization of Styrene with Circular Loop Reactor," Journal of Applied Polymer Science 39, (1990): 955-966.

Masato Tanaka, Kazuhiko Hosogai, Toshihide Yuda, Isao Kimura, Natsukaze Saito, "Preparation of Composite Particles Composed of Polystyrene and Carbon Silicide by Suspension Polymerization," Journal of the Japan Society of Colour Material 65, no. 8 (1992): 484-491.

Masato Tanaka, Kenji Hayashi, "Preparation of polystyrene particles coated with ferrite powder by suspension polymerization," Kagaku Kogaku Ronbunshu 15, no. 6 (1989): 1144-1152.

Mei-Chin Chen, Fwu-Long Mi, Zi-Xian-Liao, Kiran Sonaje, etals, "Recent advances in chitosan-based nanoparticles for oral delivery of macromolecules," Advanced Drug Delivery Reviews 65, (2013): 865-879.

Michael Betz, Barbara Steiner, Markus Schantz, Johannes Oidtmann, Karsten Mader, Elke Richling, Ulrich Kulozik, "Antioxidant capacity of bilberry extract microencapsulated in whey protein hydrogels," Food Research International 47, (2012): 51-57.

Michael Betz, Ulrich Kulozik, "Microencapsulation of bioactive bilberry anthocyanins by means of whey protein gels," Procedia Food Science 1, (2011): 2047-2056.

T. Kondo, "Saishin Maikurokapseruka Gijutsu (Microencapsulation Technique) (in Japanese)," TES. Tokyo, 1967.

Yoshinari Taguchi, Masato Tanaka, "Preparation of composite particles composed of two kinds of solid powders and waste polymer by semi-chemical recycle method," Journal of Chemical Engineering of Japan 34, no. 9 (2001): 1177-1181.

Yoshinari Taguchi, Masato Tanaka, "Preparation of composite particles made from solid powders and wasted plastics by semi chemical recycle method," Journal of Applied Polymer Science 88, (2003): 483-488.

Yoshinari Taguchi, Natsukaze Saito, Isao Kimura, Masato Tanaka, "Preparation of fine composite particles composed of inorganic solid powders and organic polymers by utilizing liquid-liquid dispersion," Colloids and Surfaces A: Physiochemical and Engineering Aspects 153, (1999): 401-404.

International Journal of Material Science (IJMSCI) Volume 4 Issue 2, June 2014 www.ij-ms.org
doi: 10.14355/ijmsci.2014.0402.03

Electrical Behaviour of Carboxy Methyl Cellulose Doped Adipic Acid Solid Biopolymer Electrolyte

M.L.H Rozali [*1], M.I.N. Isa[1, 2]

[1]Advanced Materials Group, School of Fundamental Science,
[2]Center of Corporate Communication and Image Development, Universiti Malaysia Terengganu, 21030 Kuala Terengganu, Terengganu, Malaysia

[*1]puteh89@gmail.com; [2]ikmar_isa@umt.edu.my

Received 11 March, 2014; Revised 30 April, 2014; Accepted 15 May, 2014; Published 20 June, 2014

Abstract

In this work, solid biopolymer electrolytes (SBEs) based on carboxymethyl cellulose (CMC) doped with adipic acid (AA) has been prepared by dual solvent solution casting technique. The highest room temperature ionic conductivity is 6.12 x 10^{-7} S cm^{-1} for 5 wt. % AA SBE. The temperature-dependent ionic conductivity of SBE films followed Arrhenius behaviour where R^2~1. In this system, the frequency dependent of dielectric, modulus and tangent study at various temperature and frequencies was observed to be non-Debye type. That the activation energy of relaxation is lower than the activation energy of conduction implies that the charge carrier has to overcome the higher energy barrier during conducting.

Keywords

Solid Biopolymer Electrolytes; Carboxymethyl Cellulose; Ionic Conductivity; Electrical Behaviour

Introduction

In the past two decades, the development of new solid polymer electrolyte system has been an important part in research due to the need to search for new types of electrolytes for applications in various electrochemical devices [Chai & Isa, (2011); Samsudin & Isa, (2012)]. In addition, study on natural or bio-derived polymer such as chitosan [Khiar, Puteh & Arof, (2006)], starch [Khiar & Arof, (2010)] and cellulose [Nik Aziz, Idris & Isa,(2010); Samsudin & Isa, (2012)] to be applied as biopolymer electrolytes has significantly increased due to its environmentally friendly properties [Chai & Isa, (2011); Selvasekarapandian, Hirankumar, Kawamura, Kuwata & Hattori,(2005)]. With a wide variety of biomaterial choices in the market, the rise in material cost can be avoided. Carboxymethyl cellulose (CMC) is one of cellulose derivatives which exhibit biodegradable and non-hazardous properties [Ramlli, Chai & Isa, (2013); Vieira, Avellaneda & Pawlicka, (2007)]. In its natural state, CMC is low in ionic conductivity but with the addition of proper salt and plasticizer, the ionic conductivity of CMC can be enhanced [Majid & Arof, (2007)].

This work intended on developing a new type of natural solid biopolymer electrolyte (SBE) by using CMC as the polymer host. Adipic acid (AA), an organic compound with the formula $(CH_2)_4(COOH)_2$ was used as the dopant material. The effect of temperature on conductivity, dielectric, and AC conductivity was studied to understand the behavior of the SBEs system.

Experimental

Sample Preparation

Dual-solvent solution casting technique was employed for the fabrication of the SBEs. The solvent ratio was fixed at 1:2 (ethanol:distilled water) which made up to 100 ml of total solvents. CMC (Acros Organics Co, average molecular weight 90000, D.S=0.7) was dissolved in ethanol while AA was dissolved in distilled water. Then the AA solution was added slowly into the CMC solution and continuously stirred for 3 hours until homogenous solution was obtained. The mixture solution was casted into several petri dishes and dried in the oven at 333 K for 12 hours before further drying in the desiccators. Several compositions containing different concentration of AA

(2–7 wt %) were developed using similar methods mentioned above. The composition of the samples and their designations are tabulated in Table 1.

TABLE 1: COMPOSITION OF DUAL SOLVENT

Designation	CMC (g)	AA (g)	AA (wt. %)
AA-2	2.000	0.041	2
AA-3		0.062	3
AA-4		0.083	4
AA-5		0.105	5
AA-6		0.128	6
AA-7		0.151	7

Sample Characterization

Electrical Impedance Spectroscopy

The conductivity of the CMC-AA SBEs system was measured using HIOKI 3532-50 LCR Hi-Tester interfaced to a computer in the frequency range of 50 Hz to 1 MHz and temperature of 303K to 343K. The bulk resistance, R_b was obtained from the plot of imaginary part, $-Z_i$ versus real part, Z_r of impedance. The ionic conductivity of the SBE samples can be calculated using:

$$\sigma = \frac{t}{R_b A} \quad (1)$$

where A (in cm^2) is the electrode-electrolyte contact area, R_b (in Ω) is the bulk resistance and t (in cm) is the thickness of SBE film.

Dielectric constant is a measure of the material's polarization, associated with capacity to retain stored electric charge and also represents the amount of dipole alignment in a given volume [Ramlli, Chai & Isa, (2013)]. The dielectric constant (the real part of complex permittivity, ε_r) and the dielectric loss (the imaginary part of complex permittivity, ε_i) were defined as:

$$\varepsilon_r(\omega) = \frac{Z_i}{\omega C_o (Z_r^2 + Z_i^2)} \quad (2)$$

And

$$\varepsilon_i(\omega) = \frac{Z_r}{\omega C_o (Z_r^2 + Z_i^2)} \quad (3)$$

Here, $C_o = \frac{\varepsilon_o A}{t}$ (ε_0 is the permittivity of free space, and $\omega = 2\pi f$ (f = frequency).

The real part of electrical modulus (M_r) and imaginary part of electrical modulus (M_i) were calculated using the equations below:

$$M_r(\omega) = \frac{\varepsilon_r}{(\varepsilon_r^2 + \varepsilon_i^2)} \quad (4)$$

$$M_i(\omega) = \frac{\varepsilon_i}{(\varepsilon_r^2 + \varepsilon_i^2)} \quad (5)$$

Dissipative loss can be expressed as:

$$tan\ \delta = \frac{\varepsilon_i}{\varepsilon_r}\ or\ \frac{M_i}{M_r} \quad (6)$$

Result and Discussion

Ionic Conductivity Study

The Cole-Cole plots for the sample AA-5 at room temperature is shown in Figure 1. The semicircle obtained is related to the conduction process of the polymer electrolyte. The bulk resistance (R_b) the film can be determined from the intercept high-frequency semicircle and low-frequency spike on the real axis.

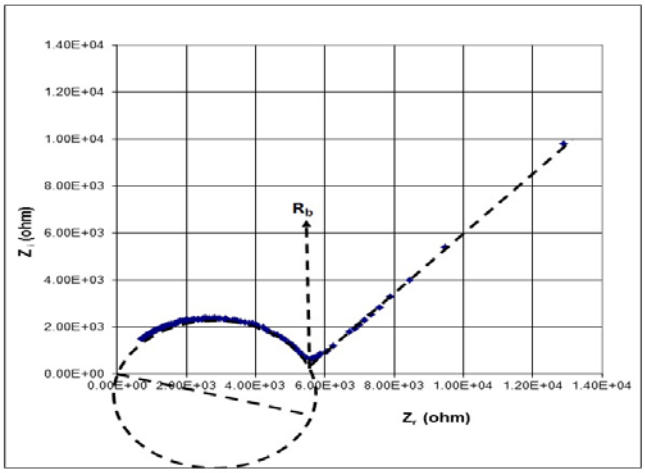

FIGURE 1: COLE-COLE PLOT FOR SAMPLE (AA-5).

Since the blocking electrodes have been used in the impedance analysis, the electrolyte or electrode interface could be regarded as a capacitance. When the capacitance is ideal, it should show a vertical spike in the impedance plot. However, the spike inclined at an angle (ɵ) less than 90^o has been found instead of the vertical spike which may be attributed to the non-homogeneity or roughness of the electrolyte or electrode interface.

The ionic conductivity depends on several factors, such as types of charge carrier (cation/anion), salt concentration and temperatures [Chai & Isa, (2011)]. Figure 2 depicts the ionic conductivity, (σ) of CMC-AA SBEs at room temperature.

It can be seen that the ionic conductivity increases with the addition of AA which can be attributed to the increase in the number of mobile charge carriers as observed by [Selvasekarapandian, Hirankumar, Kawamura, Kuwata & Hattori, (2005)]. The ionic conductivity achieved the maximum value of 6.12 x 10-

^{7} S cm^{-1} (AA-5) for 5wt% AA concentration. Above this concentration, ionic conductivity was observed to decline. According to [4], the dependence of ionic conductivity on the dopant concentration provides information on the specific interaction between ionic dopant and the polymer matrix. The decrement of ionic conductivity at higher AA concentration is attributed to the overcrowded of the ions, hence reduces the number of charge carriers and limits their mobility [Selvasekarapandian, Hirankumar, Kawamura, Kuwata & Hattori, (2005)].

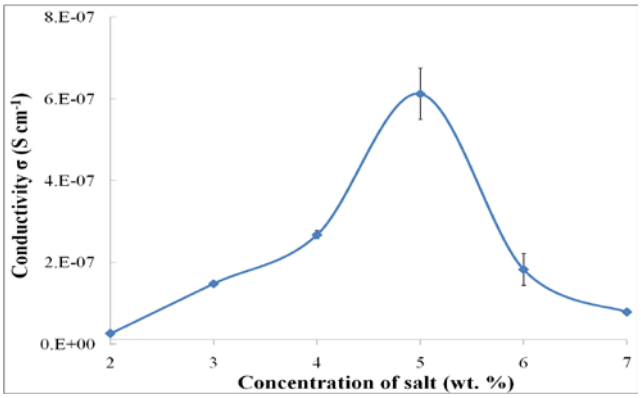

FIGURE 2: IONIC CONDUCTIVITY OF CMC- AA SOLID BIOPOLYMER ELECTROLYTES AT ROOM TEMPERATURE.

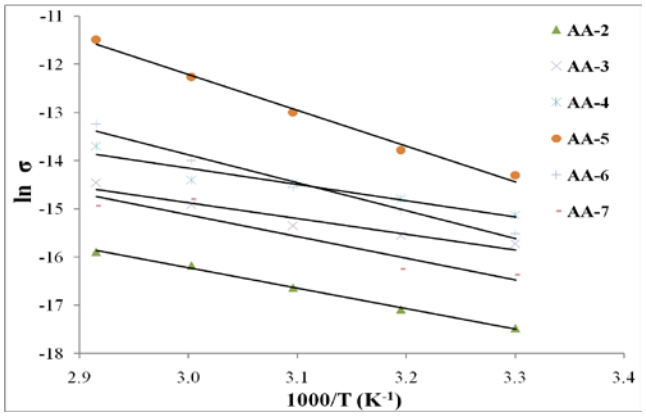

FIGURE 3: TEMPERATURE-DEPENDENT OF IONIC CONDUCTIVITY FOR CMC-AA SOLID BIOPOLYMER ELECTROLYTES

The temperature-dependent ionic conductivity was performed to analyze the ionic conduction mechanism of polymer electrolytes [Ramlli, Chai & Isa, (2013)]. Figure 3 depicts the plots of ln σ versus 1000/T for the CMC-AA SBE system and it was found to be a straight line with regression value almost unity (R^2~1) with increasing temperature which implies that SBE system follow Arrhenius behavior. The Arrhenius behaviour can be expressed by the relation of:

$$\sigma = \sigma_0 exp\ (-E_a/kT) \quad (7)$$

where σ_0 is the pre-exponential factor, E_a the activation energy and k is the Boltzmann constant and T is absolute temperature (K).

The E_a (in eV) can be retrieved from ln σ versus 1000/T for all SBE samples and is plotted in Figure 4. E_a is the sum of the energy of defect formation and the energy for migration. According to [Chai & Isa, (2011)], the decrease of E_a with addition of ionic dopant is due to the fact that the increase amount of ions in the polymer electrolytes with concentration leads to the decrease in the energy barrier for the ion transport. However for this SBEs system the E_a value is the highest at the highest conductivity. The calculated *Ea* value for sample AA-5 is 0.64 eV. In this instance, the conducting ions are more easily excited to free ion-like state, which effects on the increase of the CMC-AA SBE conductivity. Nevertheless, it can be due to the increase in number of mobile ions, diffusion coefficient of mobile ions and ionic mobility of mobile ions [Chai & Isa, (2011); Ramlli, Chai & Isa, (2013)]. The conductivity behavior of SBEs can be further explored from the dielectric studies.

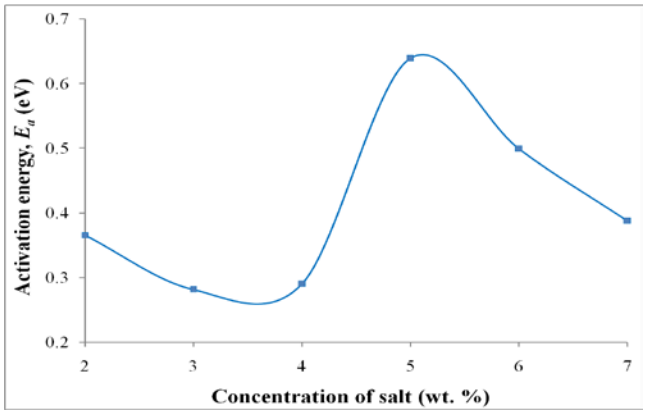

FIGURE 4: ACTIVATION ENERGY VERSUS SALT CONTENT

Dielectric Studies

The variation of dielectric constant, (ε_r) and loss, (ε_i) for the highest ionic conductivity sample (AA-5) for as a function of frequency at various temperatures are shown in Figure 5 (a) and (b).

There were no appreciable relaxation peaks observed in the frequency range. Both ε_r and ε_i rose sharply at low frequencies indicating that electrode polarization and space charge effects had occurred confirming non-Debye dependence [Khiar, Puteh & Arof, (2006)] and thus implying that the conductivity exhibits relaxation that was non-exponential in time. As the frequency increased, the rate of reversal of the electric field also increased, and so there was no time for charge to build up at the interface. Therefore, the polarization due to charge accumulation decreased that led to the decreasing in the value of dielectric loss [Khiar & Arof,

(2010)]. A further analysis of the electrical behavior would be more successfully achieved using dielectric modulus, which suppressed the effect of electrode polarization.

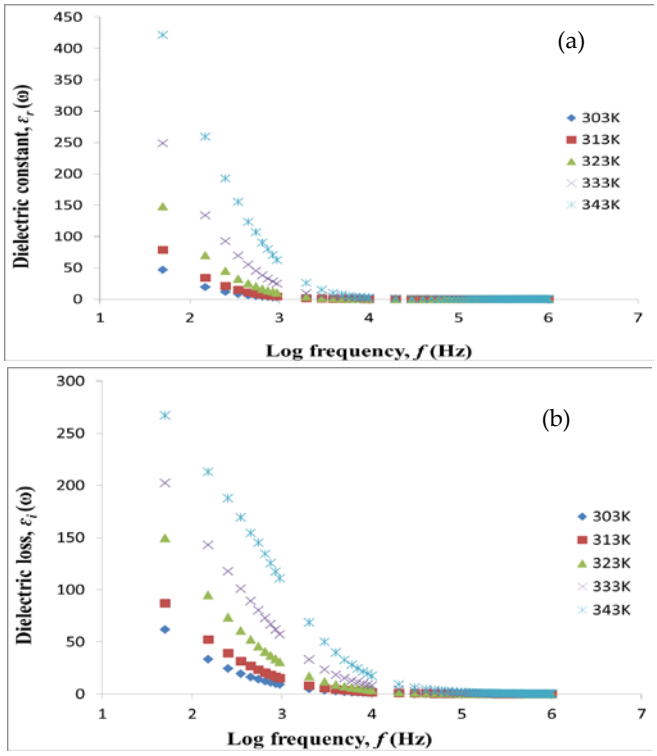

FIGURE 5: FREQUENCY DEPENDENCE OF (A) DIELECTRIC CONSTANT, AND (B) DIELECTRIC LOSS, AT VARIOUS TEMPERATURES FOR AA-5

Modulus Studies

The variations of real (M_r) and imaginary (M_i) parts of electrical modulus for the highest ionic conductivity of sample (AA-5) as a function of frequency at various temperatures are shown in Figure 6 (a) and (b) respectively.

According to [Prabakar, Narayandass & Mangalaraj, (2003)], the possible presence of peaks in the modulus formalism at higher frequencies for all SBE samples and temperature indicates that the SBE films are ionic conductors. From the Figure 6, both M_i and M_r approach to zero at low frequency and show an increase at the higher frequency without relaxation peaks (323K-343K). The plot exhibit low value at lower frequencies which might be due to the large value of capacitance associated with the electrodes. This further confirm the non-Debye behavior in the samples. The frequency range on the lower side of the peak frequency determine the range in which charge carriers are mobile over long distances [Khiar, Puteh & Arof, (2006)].

Since there are only two definitive peaks observed in the *Mi* plots in both cases, tan δ is plotted with respect to frequency for the SPE system electrolytes (Figure 7). From the figure, it can be seen that tan δ increases with frequency, passes through a maximum value and thereafter decreases. The maxima of tan δ shift towards higher frequency and the height of the peak increases with increasing temperature. This is due to the increment in number of charge carriers for conduction which decreases the resistivity of the samples [Prabakar, Narayandass & Mangalaraj, (2003); Majid & Arof, (2007)]. The loss tangent, tan δ is calculated using Equation (6).

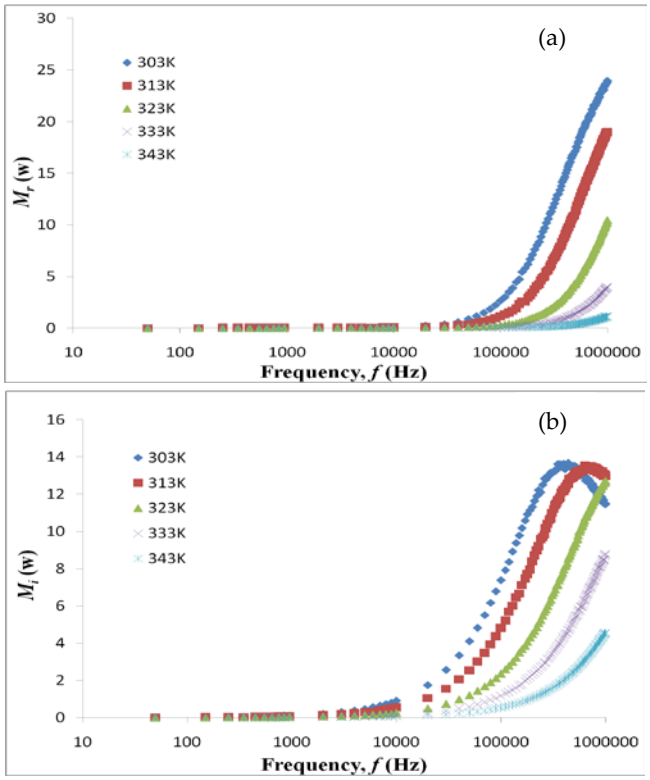

FIGURE 6: FREQUENCY DEPENDENCE OF (A) REAL PART, MR AND (B) IMAGINARY PART, MI OF MODULUS STUDY AT VARIOUS TEMPERATURES FOR SAMPLE AA-5.

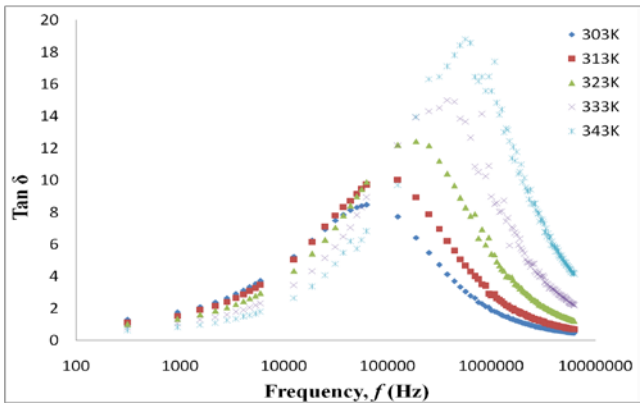

FIGURE 7: VARIATIONS OF LOSS TANGENT (TAN Δ) WITH FREQUENCY FOR SBE SAMPLE AA-5 AT VARIOUS TEMPERATURES.

According to [Karan, Pradhan, Thomas, Natesan & Katiyar, (2008)], the occurrence of relaxation time τ can be obtained from the peak of tan δ using the relation:

$$\tau = \frac{1}{\omega_{peak}} \quad (8)$$

The loss tangent peaks appearing in the plot for the sample AA-5 inferred that the H+ in the sample was more capable in following the change in the direction of applied electric field [Ramya, Selvasekarapandian, Hirankumar, Savitha & Angelo, (2008)]. Figure 8 shows the plot of *ln* τ versus 1000/T.

The temperature-dependent of relaxation times appear thermally activated and can be described by Arrhenius law:

$$\tau = \tau_o exp\left(-\frac{E_\tau}{kT}\right) \quad (9)$$

where τ_o is the pre-exponential factor and E_τ is activation energy for relexation.

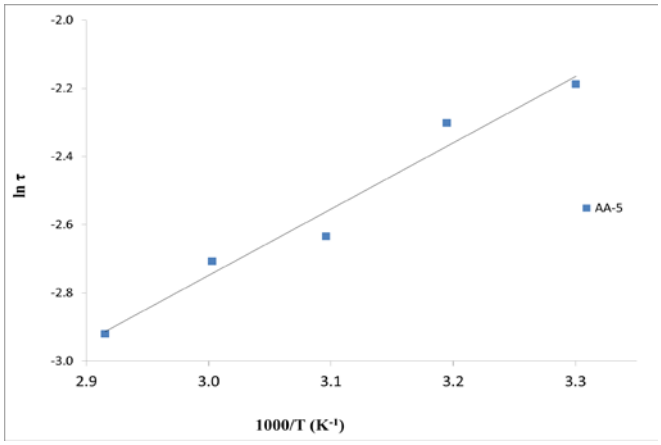

FIGURE 8: THE LINEAR GRAPH OF LN T VERSUS 1000/T FOR SBE SAMPLE AA-5.

The activation energy, for relaxation process ($E\tau$) can be obtained from the slope of plot in the Figure 8. The $E\tau$ for AA-5 was 0.17 eV. Upon comparing the values of $E\tau$ and *Ea*, it can be observed that the value of *Ea*, is higher than the value of $E\tau$. This indicates that the charge carrier has to overcome higher energy barrier while conducting comparable to relaxing [Khiar, Puteh & Arof, (2006)].

Conclusion

Carboxymethyl cellulose based solid biopolymer electrolytes with different concentration of adipic acid were prepared by dual solvent solution casting technique. The addition of adipic acid concentration was found to influence the ionic conductivity with the highest room temperature ionic conduction value 6.12 x 10^{-7} Scm^{-1} for sample containing 5 wt. % AA. The temperature dependence of ionic conductivity showed that the SBEs system exhibited Arrhenius behavior where regression value almost equal to 1. The dielectric behavior of the SBEs shows strong dependence with frequency and temperature. The activation energy was 0.64 eV and the activation energy of relaxation was 0.17 eV for sample AA-5. This implies that the charge carrier has to overcome higher energy barrier while conducting.

ACKNOWLEDGEMENT

The authors would like to thank all the members of Advanced Material Team and Ministry of Education Malaysia for financial support via FRGS and ERGS grant.

REFERENCES

Chai M.N., and Isa M.I.N., (2011) "Carboxyl methylcellulose solid polymer electrolytes: Ionic conductivity and dielectric study," Journal of Current Engineering Research, Vol. 1, pp. 23-27.

Chai, M. N., and Isa M. I. N. (2011). Carboxyl methylcellulose solid polymer electrolytes: Ionic conductivity and dielectric study. J. Curr. Eng. Res. 1(2): 23–27.

Karan NK, Pradhan DK, Thomas R, Natesan B, Katiyar RS (2008) Solid polymer electrolytes based on polyethylene oxide and lithium trifluoro- methane sulfonate (PEO–LiCF3SO3): Ionic conductivity and dielectric relaxation. Solid State Ionics. 179: 689–696.

Khiar ASA, Arof AK (2010) Conductivity studies of starch-based polymer electrolytes. Ionics.16: 123- 129.

Khiar ASA, Puteh R, Arof AK (2006) Conductivity studies of a chitosan-based polymer electrolyte. Physica B. 373: 23-27.

Majid SR, Arof AK (2007) Electrical behaviour of proton-conducting chitosan-phosphoric acid-based electrolytes. Physica B. 390: 209-215.

Nik Aziz NA, Idris NK, Isa MIN (2010) Proton conducting polymer electrolytes of methylcellulose doped ammonium fluoride: Conductivity and ionic transport studies. International journal of the physical sciences. 5(6): 748- 752.

Prabakar K., Sa.K. Narayandass, D. Mangalaraj, (2003) Dielectric and electric modulus properties of vacuum evaporated $Cd_{0.8}Zn_{0.2}Te$ thin films,Mater. Sci. Eng. B 98 225.

Ramlli M.A., Chai M.N. and Isa M.I.N. (2013) influence of propylene carbonate as a plasticizer in CMC OA based biopolymer electrolytes: conductivity and electrical study Advanced Materials Research Vol. 802 (2013) pp 184-188.

Ramya CS, Selvasekarapandian S, Hirankumar G, Savitha T, Angelo PC (2008) Investigation on dielectric relaxations of PVP–NH4SCN polymer electrolyte. Journal of Non-Crystalline Solids. 354: 1494–1502.

Samsudin, A.S. & Isa, M.I.N. (2012). Structural and ionic transport study on CMC doped NH4Br: A new types of biopolymer electrolytes. Journal of Applied Sciences, 12, 174-179.

Selvasekarapandian S, Hirankumar G, Kawamura J, Kuwata N, Hattori T (2005) H solid state NMR studies on the proton conducting polymer electrolytes. Materials Letters. 59: 2741-2745.

Vieira DF, Avellaneda CO, Pawlicka A (2007) Conductivity study of a gelatin-based polymer electrolyte.ElectrochimicaActa. 53: 1404-1408.

Mohd Lukhman Hakim Rozali (M.L.H Rozali) was born in Kuala Terengganu, Terengganu, Malaysia in 1989. He received his B.Sc. App. degree in physic electronics and instrumentation from Universiti Malaysia Terengganu, Malaysia, in 2011, and then studying his M.S. degree in physics in 2012 in Universiti Malaysia Terengganu, Malaysia, from 2012. This is the 2nd year of his M.S. study. His current research interests is biopolymer electrolytes and has published in SCI journals and attended The Regional Conference of Solid State Science and Technology (RCSSST) conference held in Sabah, Malaysia.

Mohd Ikmar Nizam Mohammad Isa (M.I.N Isa) was born in Kuala Lumpur, Malaysia in 1978. He received his B.Sc.App. degree in computational physics and electronics 2002 and Ph.D. degree 2006 from Department of Physics, University of Malaya. In 2006 his start working at Universiti Malaysia Terengganu, Associate Professor Dr. Ikmar Nizam worked as director of corporate communication and image development centre and physics senior lecturer. His research has been focused on advanced material science, solid state ionics and environmental energy. Since the energy issue is getting more and more important part of his research has been focused on the development of proton battery in the past 7 years.

International Journal of Material Science (IJMSCI) Volume 4 Issue 2, June 2014 www.ij-ms.org
doi: 10.14355/ijmsci.2014.0402.04

Rational Approach for Material Selection in FRP-Bonded Reinforced Concrete Repair

Hasan Nikopour[1], Moncef Nehdi*[2]

[1]Department of Civil Engineering and Applied Mechanics, McGill University, Montreal, QC, Canada H3A 2K6,
*[2]Department of Civil and Environmental Engineering, Western University, London, Ontario, Canada, N6A 5B8,
hasan.nikopourdeilami@mail.mcgill.ca; mnehdi@eng.uwo.ca

Received 20 January, 2014; Revised 3 April, 2014; Accepted 30 April, 2014; Published 20 June, 2014

Abstract

Fibre-reinforced polymers (FRP) wraps have shown great promise in the retrofit and rehabilitation of ageing and damaged reinforced concrete (RC) elements. After nearly four decades of research in this area, the FRP material selection for a particular repair application is still a challenge in the research and industrial communities. This paper presents novel approaches for selecting the optimum FRP choice from a list of candidate materials.

Keywords

Material Selection; Repair; Reinforced Concrete; Fibre-Reinforced Polymer

Introduction

A considerable inventory of existing concrete structures needs to be retrofitted due to one or more of the following causes: (1) improper quality of materials, (2) incorrect specifications, (3) faulty design, (4) errors in the construction process, and (5) exposure of structures to extreme loading and/or environmental conditions. Chemical and physical agents may induce a gradual increase in concrete porosity and permeability. Low-cycle fatigue and freeze-thaw cycles can compromise further the material integrity, allowing chemical substances to penetrate concrete. The corrosion of the reinforcing steel results in the formation of expansive products, generating internal stresses and subsequent cracking and spalling of the concrete. Such problems can lead to insufficient structural capacity that can decrease the service life of a structure [Shash, 2005]. A typical deteriorated concrete bridge deck is shown in Fig. 1.

A relatively new progress in the repair and rehabilitation of RC elements is the use of externally bonded FRP composite wraps (Fig. 2). FRPs have received great attention and their applications to structural repair and retrofit have grown significantly in recent years. FRPs have proven to be an excellent option for the external reinforcement of concrete because of their high tensile strength, lightweight, resistance to corrosion, high durability, and ease of installation [Nikopour and Nehdi, 2011].

FIG. 1 EXAMPLEOFDAMAGED-DETERIORATED BRIDGE DECK (with permission-http://www.eng.cam.ac.uk).

FIG. 2 APPLICATION OF EXTERNAL CFRP WRAPFORREPAIRING A RC BEAM (with permission-http://www.fyfeco.com).

Although, the concept of composite materials, which are basically a combination of two or more materials to

obtain a new material, has been known for thousands of years (Fig. 3), the idea of modern fibre-reinforced composites dates back to a few decades ago. Modern FRPs are constructed of high-performance fibres such as carbon, aramid, or glass, which are placed in a resin matrix. The variety of FRPs is not just limited to fibre and matrix material properties. The geometry, lay-up and manufacturing process are also key variables in forming various types of FRPs (Fig. 4). By selecting from the many available fibres, geometries and polymers, the mechanical and durability properties can be tailored for a particular application [Hull, 1996].

FIG. 3 KABOUTAR-KHANEH, ASTRUCTURE MADE OF MALT-STRAW COMPOSITE IN THE 13th CENTURY, YAZD, IRAN.

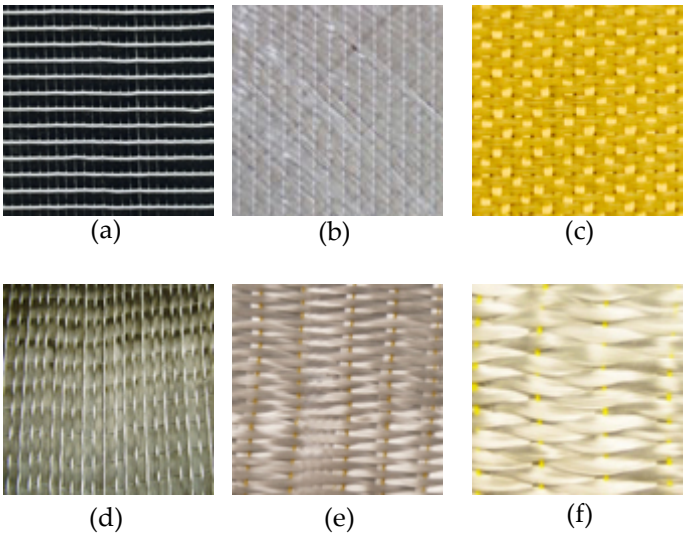

Fig. 4 VARIOUS FRP TYPES (a) UNIDIRECTIONAL CARBON-FRP, (b) BIDIRECTIONAL ±45o GLASS-FRP, (c) BIDIRECTIONAL 0o/90o ARAMID-FRP, (d) BIDIRECTIONAL 0o/90oCARBON-FRP, (e) BIDIRECTIONAL 0o/90oHYBRID GLASS-ARAMID-FRP, (f) WOVENGLASS-FRP.

Generally, current design guidelines ignore the effect of the environmental and durability parameters in selecting the FRP material and only propose empirical or semi-empirical equations for estimating the ultimate strength of a repaired concrete element based on the mechanical properties of the externally bonded FRP used [Nehdi and Nikopour, 2011; Colotti*et. al.*, 2005]. Moreover, design codes ignore the effect of transverse mechanical properties of the external FRP, which can have significant effects, in particular for RC elements subjected to seismic loading [Selvadurai and Nikopour, 2012a; Selvadurai and Nikopour, 2012b; Nikopour and Selvadurai, 2013, Nikopour, 2013]. Accordingly, the main objective of this study is to introduce simple, yet effective methods for selecting the optimum FRP material for different repair applications considering cost, corrosion resistance, density and longitudinal/transverse mechanical properties of FRPs.

Materials Selection Methods

A comprehensive review of available approaches for materials selection can be found in the text by [Ashby *et. al.*, 2004]. These methods include free searching based on quantitative analysis [Ashby, 1992], checklist/questionnaire based on expertise [Tretheweyet. *al.*, 1998], and inductive reasoning and analog procedure [Amen and Vomacka, 2001]. There are also materials selection methods based on neural networks [Takuma*et. al.*, 1994], the fuzzy logic approach [Sarafraz*et. al.*, 2008], and fuzzy multi-criteria decision making [Liao, 1996]. A variety of quantitative selection procedures are also available to analyze the large amount of data involved in the materials selection processes [Fayazbakhsh*et. al.*, 2009]. The various steps of material selection process are illustrated in a chart (Fig. 5). The focus of this paper is on quantitative materials selection procedures.

The weighted-properties method (WPM) was proposed by [Farag, 1997]. In this method, each material property is given a certain weight, depending on its importance to the performance of the part in service. A weighted-property value is obtained by multiplying the numerical values of each property by its weighting factor, □. The individual weighted-property values of each material are then summed to calculate the comparative materials performance index, □.In cases where numerous material properties are specified and the relative importance of each property is not clear, determinations of the weighting factors, □,is largely intuitive, which reduces the reliability of WPM.

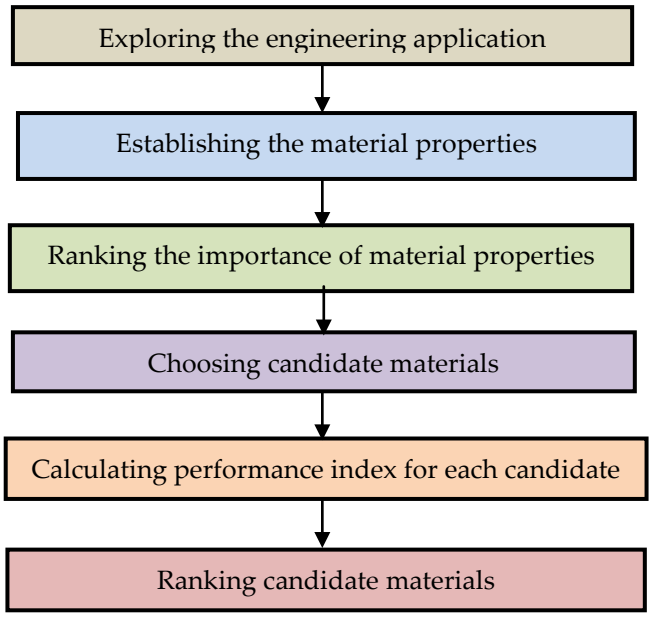

FIG. 5 STEPS OF MATERIAL SELECTION PROCESS.

The problem of ambiguity in selecting weighting factors was solved by introducing the Digital Logic (DL) approach [Farag, 1997]. In the DL technique, material properties are arranged such that only two properties are compared at a time. In comparing two properties, the more important property is given the numerical number (1) and the less important one is given (0). The relative emphasis coefficient or weighting factor, □,for each property is obtained by dividing the number of positive decisions for each goal into the total number of possible decisions, *N*. Then, each property is linearly scaled in a way that its best possible numerical value is 100. When evaluating a list of candidate materials, one property is considered at a time. The highest value in the list is rated as 100 and the others are scaled proportionally. Introducing the scaling factor, □, facilitates the conversion of normal material property values to scale dimensionless values. Equations 1 and 2 are used when the highest and lowest property values are the best choices, respectively.

$$\beta = \text{Scaled Property} = \frac{\text{Numerical Value of Property x 100}}{\text{Max. Value in List}} \quad (1)$$

$$\beta = \text{Scaled Property} = \frac{\text{Min. Value in List x 100}}{\text{Numerical Value of Property}} \quad (2)$$

After scaling the different properties, the material performance index,□, is calculated as follows:

$$\gamma = \sum_{i=1}^{n} \beta_i \alpha_i \quad (3)$$

The DL method was modified by Menshadi et al. [Manshadi*et. al.*, 2007] to what is known as the Modified Digital Logic (MDL) approach. In this method, the property evaluation was changed in a way that a value of (1) is assigned to the less important property and a value of (3) to the more important one, when two properties are considered at a time. By doing this, the least important property, which is at times eliminated in the DL technique by the property evaluation system, still remains in the selection list. Another advantage of the MDL over the DL approach is that two properties with equal importance can have equal numerical values of (2). In addition, the linear scaling of properties by the DL method (Eqs. 1 and 2) were replaced by two different nonlinear functions, for normalization purposes, as presented in Eqs. 4 and 5:

$$\begin{cases} \beta = a_1 \ln(b_1 X + c_1) & \text{for } X_C \neq X_{\max}/2 \\ \beta = \dfrac{200X}{X_{\max}} - 100 & \text{for } X_C = X_{\max}/2 \end{cases} \quad (4)$$

$$\begin{cases} \beta = a_2 \ln(\dfrac{b_2}{X} + c_2) & \text{for } X_C \neq 2X_{\min} \\ \beta = \dfrac{200X_{\min}}{X} - 100 & \text{for } X_C = 2X_{\min} \end{cases} \quad (5)$$

where□is the scaled property, X is the value of each property, and a_1, a_2, b_1, b_2, c_1 and c_2, are constants. Equations 4 and 5 are used when the highest value and lowest value of the property, respectively, are of primary concern. The existing constants in these equations are determined by boundary conditions and information obtained from X_C .The parameter X_C , which is user defined, is used to assign a critical value to each property less than which the scaled property becomes negative. The constants a_1, a_2, b_1, b_2, c_1 and c_2, are calculated using six equations available in [Manshadi *et. al.*, 2007]. The dependence of the method on X_C , the indefiniteness of some of the introduced constants in some cases, and the unstandardized scaling of the properties are the main disadvantages of the MDL method [Fayazbakhsh *et. al.*, 2009].

More recently, Z-transformation scaling, which has its roots in statistics, was proposed for replacing the nonlinear scaling functions in the MDL method [Fayazbakhsh *et. al.*, 2009]. In this approach, the same weighting factors, □,of the MDL method are used. However, for scaling purposes, Eq. 6 was introduced, where the positive and negative signs are used when higher value and lower value of a property, respectively, are desirable.

$$\beta = \pm \frac{X - \mu}{\sigma} \quad (6)$$

where X is the value of material property, $\sigma$is the

standard deviation, and $\mu$is the mean of each property for the list of candidate materials.

In the present study, the DL, MDL and Z-transformation methods have been used in comparing a list of 6 candidate materials encompassing various types of unidirectional or hybrid FRPs. For further clarification, a case study has been conducted for repairing damaged reinforced concrete beams in normal and extremely salty exposure environments and the findings are presented herein.

Case Study

A typical civil engineering rehabilitation project of a bridge was selected. In this case study, it was decided to use a typical supporting beam, which had exhibited deterioration. In general practice, the strengthening of the beam is done by repairing surface damage with new concrete and attaching structural steel plates or external FRP wraps on the exposed surfaces. The steel plate is usually bolted into place, whereas the FRP wraps are epoxy bonded to develop the required anchorage. Two environmental exposure situations were considered: a normal dry exposure with no possibility of environmental or chemical attack (Case-1) and an extremely salty environment with high possibility of chloride and sulphate ions chemical exposure (Case-2). Six different carbon and glass FRP wraps were selected as candidate materials (Table 1). DL, MDL and Z-transformation material selection methods were used in ranking the candidate materials based on seven mechanical, physical and economical properties.

Tables 2 and 3 present the determination of weighting factors, $\square$, based on the DL method for Case-1 and Case-2, respectively. As shown, in Case-1, the DL method eliminated corrosion resistance, and in Case-2, the effect of cost was eliminated from the selection criteria. The MDL and Z-transformation methods used identical weighting factors, which are presented in Tables 4 and 5 for the two environmental cases, respectively. In contrast with the DL method, there was no possibility of elimination of any selection criteria in the MDL and Z-transformation approaches. In Case-1, the longitudinal strength had the maximum weight, whereas in Case-2, the corrosion resistance had the maximum weight.

Tables 6 to 8 show the calculated scaled properties, $\square$, based on various methods. It should be mentioned that scaled properties are independent of the environmental exposures selected. Corrosion resistance qualitative parameters, excellent and good, were converted to values of (2) and (1), respectively, in order to calculate their quantitative scaled representations.

Table 9 summarizes the performance index and ranking of candidate materials based on the DL, MDL and Z-transformation methods for the normal environmental exposure (Case-1). Candidate material C (SikaWrap 900C) obtained the first rank based on all three material selection approaches. The main disadvantage of this candidate was its cost, while it had superior longitudinal strength/modulus, density and corrosion resistance properties. Table 10 summarizes the performance index and ranking of candidate materials based on the DL, MDL and Z-transformation methods for the extremely salty environmental exposure (Case-2). The rankings of the MDL and Z-transformation methods were nearly identical in both environmental exposure cases. However, the DL method ranking order had considerable variation.

Uncertainties in Material Properties

The classic material selection methods considered consist of: m candidate materials (M_i; i = 1,..., m); n design criteria (scaled material properties $\square_j$;j = 1,...,n); and n weighting factors ($\square_j$;j = 1,..., n). In order to account for possible uncertainties in material property values, a set of threshold values should also be added to the above list. Consequently, the problem with uncertainly furthermore consists of: n strict preference thresholds (p_j; j = 1,..., n), reflecting the upper limit of uncertainty in each scaled material property value; and n indifference preference thresholds (q_j; j = 1,..., n), reflecting the lower limit of uncertainty in each criterion value; and n veto thresholds (v_j; j = 1,..., n), each of which reflecting a maximum allowable limit for a veto condition [Milani and Shanian, 2006].

For each criterion, $q_j \le p_j \le v_j$. To solve the material selection problem with uncertain material properties, ELECTRE III [Roy, 1990; Milani and Shanian, 2006], a pseudo-criterion definition instead of a classical definition can be used with conjunction of Z-transformation method. Each material has one indifference zone with a range of ($-q_i$, q_i) through which no preference relation may be made. There is also a strict preference zone, ($-p_i$, p_i), beyond which a strong preference can be noticeable.

TABLE 1 CANDIDATE MATERIALS PROPERTIES

Candidate Material	Longitudinal strength (MPa)	Longitudinal modulus (GPa)	Transverse strength (MPa)	Transverse modulus (GPa)	Density (g/cm³)	Price ($/m²)	Corrosion resistance
A (SikaWrap 230C)	894	65.4	27	5.8	1.8	38.55	Excellent
B (SikaWrap 103C)	849	70.5	24	4.8	1.8	81.63	Excellent
C (SikaWrap 900C)	1120	100.0	30	7.3	1.8	100.10	Excellent
D (SikaWrap 430G)	537	26.4	23	7.0	2.54	9.10	Good
E (Sikawrap 100G)	612	26.1	30	6.6	2.54	13.43	Good
F (SikaWrap 107G)	648	26.1	50	8.5	2.54	13.80	Good

TABLE 2 DETERMINATION OF WEIGHTING FACTORS (α) FOR A NORMAL EXPOSURE (CASE-1) BASED ON THE DL METHOD

Goals	Number of possible decisions [$N = n(n-1)/2$]																					Positive decisions	α
	1	2	3	4	5	6	7	8	9	10	11	12	13	14	15	16	17	18	19	20	21		
Longitudinal strength	1	1	1	1	0	1																5	0.238
Longitudinal modulus	0						1	1	1	0	1											4	0.190
Transverse strength		0					0					1	1	0	1							3	0.143
Transverse modulus			0					0				0				1	0	1				2	0.095
Density				0					0				0			0			0	1		1	0.047
Cost					1					1				1			1		1		1	6	0.287
Corrosion resistance						0					0				0			0		0	0	0	0.000

TABLE3 DETERMINATION OF WEIGHTING FACTORS (α) FOR ASEVEREEXPOSURE (CASE-2) BASED ON THE DL METHOD

Goals	Number of possible decisions [$N = n(n-1)/2$]																					Positive decisions	α
	1	2	3	4	5	6	7	8	9	10	11	12	13	14	15	16	17	18	19	20	21		
Longitudinal strength	1	1	1	1	0	0																4	0.190
Longitudinal modulus	0						1	1	1	0	0											3	0.143
Transverse strength		0					0					1	1	0	0							2	0.095
Transverse modulus			0					0				0				1	0	0				1	0.047
Density				0					0				0			0			0	0		0	0.000
Cost					1					1				1			1		1		0	5	0.238
Corrosion resistance						1					1				1			1		1	1	6	0.287

TABLE4 DETERMINATION OF WEIGHTING FACTORS (α) FOR A NORMAL EXPOSURE (CASE-1) FOR THE MDL AND Z-TRANSFORMATION METHODS

Goals	Number of possible decisions [$N = n(n-1)/2$]																					Positive decisions	α
	1	2	3	4	5	6	7	8	9	10	11	12	13	14	15	16	17	18	19	20	21		
Longitudinal strength	3	3	3	3	2	3																17	0.202
Longitudinal modulus	1						3	3	3	2	3											15	0.179
Transverse strength		1					1					3	3	1	3							12	0.143
Transverse modulus			1					1				1				3	1	3				10	0.119
Density				1					1				1			1			1	3		8	0.095
Cost					2					2				3			3		3		3	16	0.190
Corrosion resistance						1					1				1			1		1	1	6	0.072

TABLE5 DETERMINATION OF WEIGHTING FACTORS (α) FOR ASEVEREEXPOSURE (CASE-2) FOR THE MDL AND Z-TRANSFORMATION METHODS

Goals	Number of possible decisions [$N = n(n-1)/2$]																					Positive decisions	α
	1	2	3	4	5	6	7	8	9	10	11	12	13	14	15	16	17	18	19	20	21		
Longitudinal strength	3	3	3	3	2	1																15	0.179
Longitudinal modulus	1						3	3	3	2	1											13	0.155
Transverse strength		1					1					3	3	1	1							10	0.119
Transverse modulus			1					1				1				3	1	1				8	0.095
Density				1					1				1			1			1	1		6	0.071
Cost					2					2				3			3		3		1	14	0.167
Corrosion resistance						3					3				3			3		3	3	18	0.214

TABLE 6 SCALED PROPERTY VALUES, β, PERFORMED BY THE DL METHOD

Candidate Material	Longitudinal strength	Longitudinal modulus	Transverse strength	Transverse modulus	Density	Cost	Corrosion resistance
A (SikaWrap 230C)	79.82	71.71	54.00	68.23	100.00	23.60	100.00
B (SikaWrap 103C)	75.80	76.64	48.00	56.47	100.00	11.14	100.00
C (SikaWrap 900C)	100.00	100.00	60.00	85.88	100.00	9.09	100.00
D (SikaWrap 430G)	47.94	15.51	46.00	82.35	70.86	100.00	50.00
E (SikaWrap 100G)	54.64	14.85	60.00	77.64	70.86	67.75	50.00
F (SikaWrap 107G)	57.85	14.85	100.00	100.00	70.86	65.94	50.00

TABLE 7 SCALED PROPERTY VALUES, β, PERFORMED BY THE MDL METHOD

Candidate Material	Longitudinal strength	Longitudinal modulus	Transverse strength	Transverse modulus	Density	Cost	Corrosion resistance
A (SikaWrap 230C)	65.98	71.71	27.21	41.42	100.00	70.54	100.00
B (SikaWrap 103C)	58.90	76.64	15.91	18.66	100.00	40.41	100.00
C (SikaWrap 900C)	100.00	100.00	38.01	74.46	100.00	29.62	100.00
D (SikaWrap 430G)	6.61	15.51	12.03	67.95	51.23	100.00	46.49
E (SikaWrap 100G)	19.72	14.85	38.01	59.20	51.23	91.33	46.49
F (SikaWrap 107G)	25.89	14.85	100.00	100.00	51.23	90.41	46.49

TABLE 8 SCALED PROPERTY VALUES, β, PERFORMED BY Z-TRANSFORMATION METHOD

Candidate Material	Longitudinal strength	Longitudinal modulus	Transverse strength	Transverse modulus	Density	Cost	Corrosion resistance
A (SikaWrap 230C)	0.537	0.418	-0.369	-0.680	0.912	0.107	0.912
B (SikaWrap 103C)	0.331	0.582	-0.672	-1.465	0.912	-0.993	0.912
C (SikaWrap 900C)	1.573	1.532	-0.067	0.497	0.912	-1.465	0.912
D (SikaWrap 430G)	-1.098	-0.837	-0.773	0.261	-0.912	0.860	-0.912
E (SikaWrap 100G)	-0.754	-0.847	-0.067	-0.052	-0.912	0.750	-0.912
F (SikaWrap 107G)	-0.589	-0.847	1.950	1.439	-0.912	0.740	-0.912

TABLE 9PERFORMANCE INDEX AND RANKING OF CANDIDATE MATERIALS IN A NORMAL EXPOSURE ENVIRONMENT (CASE-1) USING THE DL, MDL, AND Z-TRANSFORMATION METHODS

Candidate Material	DL method		MDL method		Z-transformation method	
	Performance index (γ)	Rank	Performance index (γ)	Rank	Performance index (γ)	Rank
A (SikaWrap 230C)	58.29	4	65.09	2	0.222	2
B (SikaWrap 103C)	52.72	6	54.50	4	-0.136	4
C (SikaWrap 900C)	66.84	1	74.72	1	0.515	1
D (SikaWrap 430G)	60.78	3	41.13	6	-0.440	6
E (SikaWrap 100G)	54.55	5	44.68	5	-0.329	5
F (SikaWrap 107G)	62.64	2	59.47	3	0.168	3

TABLE 10PERFORMANCE INDEX AND RANKING OF CANDIDATE MATERIALS IN A SEVERE EXPOSURE ENVIRONMENT (CASE-1) USING THE DL, MDL, AND Z-TRANSFORMATION METHODS

Candidate Material	DL method		MDL method		Z-transformation method	
	Performance index (γ)	Rank	Performance index (γ)	Rank	Performance index (γ)	Rank
A (SikaWrap 230C)	68.07	2	70.38	2	0.330	2
B (SikaWrap 103C)	63.92	3	61.34	3	0.024	3
C (SikaWrap 900C)	73.89	1	78.44	1	0.573	1
D (SikaWrap 430G)	57.71	4	41.76	6	-0510	6
E (SikaWrap 100G)	52.32	6	44.81	5	-0.414	5
F (SikaWrap 107G)	57.35	5	57.02	4	-0.004	4

Based on the difference in the positions of two given options such as M_i, M_k on the criterion axes, one can infer one of three cases as follows. One is considered indifferent to another, there is a weak preference of one to another, or there exists a strong preference of one over another. For each pair of materials such as (M_i, M_k), a fuzzy outranking relation can be built in the ELECTRE III procedure. This is done by introducing a credibility degreeδ_{ik}which represents the credibility of the outranking relation of M_i and M_k. The credibility degree is defined by using the concordance c_j (M_i, M_k) and discordance d_j (M_i, M_k) indices with respect to the

scaled material property, β_j.

The concordance index allows the solution mechanism to verify whether M_i is at least as good as M_k with respect to the jth design criterion. On the other hand, the discordance index verifies if there exists a very high opposition to the outranking relation of M_i and M_k. Thus, materials with very weak performances in one or more design criteria are always in risk of being vetoed against their outranking relations. The concordance index increases linearly from its minimal value when $\beta_j(M_k) - \beta_j(M_i)$ passes the strict preference threshold p_j and reaches to its maximum value when $\beta_j(M_k) - \beta_j(M_i)$ is within the indifference zone identified by q_j. This can be explicitly formulated by,

$$c_j(M_i, M_k) = \begin{cases} 0 & ; p_j < \beta_j(M_k) - \beta_j(M_i) \\ \dfrac{\beta_j(M_k) + p_j - \beta_j(M_i)}{p_j - q_j} & ; q_j < \beta_j(M_k) - \beta_j(M_i) \le p_j \\ 1 & ; \beta_j(M_k) - \beta_j(M_i) \le q_j \end{cases} \quad (7)$$

Note that the presented relation uses the convention that β_j needs to be maximized. Similarly, the discordance index increases linearly from its minimal value when $\beta_j(M_k) - \beta_j(M_i)$ is below the strict preference threshold p_j and reaches to its maximum value when $\beta_j(M_k) - \beta_j(M_i)$ outreaches the veto threshold v_j:

$$c_j(M_i, M_k) = \begin{cases} 0 & ; \beta_j(M_k) - \beta_j(M_i) < p_j \\ \dfrac{\beta_j(M_k) + p_j - \beta_j(M_i)}{v_j - p_j} & ; p_j \le \beta_j(M_k) - \beta_j(M_i) \le v_j \\ 1 & ; v_j < \beta_j(M_k) - \beta_j(M_i) \end{cases} \quad (8)$$

For an ideal alternative, M_i^*, one expects $c_j(M_i^*, M_k) = 1$ and $d_j(M_i^*, M_k) = 0$ for all k; $k \neq i$. Following the solution process, the $c_j(j = 1,2,...,n)$ indices are aggregated in a global concordance index as:

$$C_{ik} = \sum_{j=1}^{n} \alpha_j c_j(M_i, M_k) \quad (9)$$

Finally, the credibility degree for the pair of materials is calculated by:

$$\delta_{ik} = C_{ik} \prod \frac{1 - d_j(M_i, M_k)}{1 - C_{ik}} \quad (10)$$

Where $\bar{F}$ is defined as $\bar{F} = \{ j \mid j \in F, d_j(M_i, M_k) > C_{ik} \}$ and $\bar{F} \subset F \equiv \{1,2,...,n\}$. In Eq. (10) when at least one $d_j(M_i, M_k) = 1$, $\delta_{kl} = 0$. The latter clearly constitutes the non-compensatory aspect of the ELECTRE approach via the veto condition. It implies that if material M_i is very poor as compared to M_k with regards to only one particular design criterion (i.e., $v_j < \beta_j(M_k) - \beta_j(M_i)$), it will not be preferred over M_k, regardless of its performance in the other criteria. The measure of such a veto condition is the threshold value, v_j, and should be pre-defined by careful analysis.

After calculating all credibility degrees for each and every pair of materials with respect to all criteria, fuzzy outranking relations [Roy, 1990; Milani and Shanian, 2006] can be established, this time between pairs of credibility degrees. The final classification of alternatives is then based on building two complete pre-orders such as Z_1 and Z_2 through descending and ascending distillation procedures. Recall that a pre-order is a relation (here the material dominance) that is reflexive and transitive but not anti-symmetric (i.e., indifferent solutions are allowed). A pre-order is complete when no incomparability between two solutions is allowed [Collette *et. al.*, 2003]. The final pre-order Z is built by intersecting the two complete pre-orders, $Z = Z_1 \cap Z_2$.

Ranking of candidate materials shown in Table 1 was done based on the discussion of the ELECTRE III approach and using weighting and scaled properties obtained from the Z-transformation method (Tables 4, 5 and 8) for two environmental cases presented earlier. q_j, p_j, v_j were set to be 0.1, 0.5 and 1.0 for all scaled properties. Table 11 summarizes the ranking of candidate materials with uncertain material properties.

Conclusions

The DL, MDL and Z-transformation methods have been used in the present study for ranking 6 candidate materials based on 7 mechanical, physical and economical parameters for a retrofitting project of a typical concrete beam under normal and extremely salty exposure environments. The following conclusions can be drawn from this research:

1. In both cases, normal and severe environmental exposure conditions, the DL method eliminates one of the selection criteria; and therefore, it is not recommended for solving similar problems.

2. For the range of material properties used in this study, the MDL and Z-transformation methods provide similar ranking of the candidate materials.

3. In the Z-transformation method, there is no need for defining the parameter X_C used in the MDL method. This greatly reduces the dependency of the method on the user knowledge.

4. The ELECTRE III multi-criteria decision model is capable of ranking candidate materials while estimating their incomparability and indifferences. The use of fuzzy outranking relations and pseudo criteria in ELECTRE III can be particularly useful to account for material data uncertainty.

REFERENCES

Amen R., and Vomacka P. "Case-based reasoning as a tool for materials selection." Mater Des 22 (2001):353-8.

Ashby M.F. "Materials Selection in Mechanical Design." Pergamon Press, New York, USA, 1992.

Ashby M.F., Brechet Y.J.M., Cebon D., and Salvo L. "Selection strategies for materials and processes." Mater Des 25 (2004):51-67.

Collette Y., and Siarry P. "Multiobjective Optimization." Springer-Verlag, New York, USA, 2003.

Colotti V., Spadea G., and Swamy N. "Analytical model to evaluate failure behaviour of plated reinforced concrete beams strengthened for shear." ACI Struct J 101 (2005):755-65.

Farag M. "Materials Selection for Engineering Design." Prentice-Hall, New Jersey, USA, 1997.

Fayazbakhsh K., Abedian A., Manshadi B.D., and Sarfaraz Khabbaz R. "Introducing a novel method for materials selection in mechanical design using Z-transformation in statistics for normalization of material properties." Mater Des30 (2009):4396-404.

Hull D. "An Introduction to Composite Materials." Cambridge University Press, Cambridge, UK, 1996.

Liao T.W. "A fuzzy multi criteria decision making method for material selection." J Manuf Syst 1996; 15:1-12.

Manshadi B.D., Mahmudi H., Abedian A., and Mahmudi R. "A novel method for materials selection in mechanical design: combination of nonlinear normalization and a modified digital logic method." Mater Des 28 (2007):8-15.

Milani A.S., and Shanian A. "Gear material selection with uncertain and incomplete data. Material performance indices and decision aid model." Mater Des 3 (2006):209-22.

Nehdi M., and Nikopour H. "Genetic algorithm model for shear capacity of RC beams reinforced with externally bonded FRP." J Mater Struc 44 (2011):1249-58.

Nikopour H. "A virtual frame work for prediction of effect of voids on transverse elasticity of a unidirectionally reinforced composite." Comput Mat Sci 79 (2013): 25-30.

Nikopour H., and Nehdi M. "Shear repair of RC beams using epoxy injection and hybrid external FRP." Mater Struct 44 (2011):1865-77.

Nikopour H., Selvadurai A.P.S. "Torsion of a layered composite Strip." Compos Struct 95 (2013):1-4.

Roy B. "Decision aid and decision making. In: Bana e Costa CA (ed.) Reading in Multiple Criteria Decision Aid." Springer-Verlag, Heidelberg, Germany, 1990.

Sarfaraz Khabbaz R., Dehghan Manshadi B., Abedian A., and Mahmudi R. "A simplified fuzzy logic approach for materials selection in mechanical engineering design." Mater Des 30 (2008):687-97.

Selvadurai A.P.S., and Nikopour H. "Transverse elasticity of a unidirectionally reinforced composite with an irregular fibre arrangement: experiments, theory and computations." Compos Struct 94 (2012a):1973-81.

Selvadurai A.P.S., and Nikopour H. "Uniform loading of a cracked layered composite plate: Experiments, and computational modelling." CMES: Computer Modeling in Engineering & Sciences 85 (2012b):279-97.

Takuma M., Shibasaka T., Teshima T., Iwai Y., and Honda T. "Study on support system for materials selection in the design process." Trans JSME C 60 (1994):294-300.

Trethewey K.R., Wood R.J.K., Puget Y., Roberge and P.R., "Development of a knowledge based system for materials management." Mater Des 19 (1998):39-56.

doi: 10.14355/ijmsci.2014.0402.06

Substrate Temperature Influenced Physical and Electrochromic Properties of MoO3 Thin Films

S. Subbarayudu*, V. Madhavi, S. Uthanna

Department of Physics, Sri Venkateswara University, Tirupati - 517 502, India

*srsuguru.phy@gmail.com; madhuvphysics@gmail.com; uthanna@rediffmail.com

Received 24 June, 2013; Revised 4 February, 2014; Accepted 3 March, 2014; Published 20 June, 2014

Abstract :

Molybdenum oxide (MoO_3) films were deposited on glass and silicon substrates by sputtering of molybdenum target at different substrate temperatures in the range 473-573 K at a constant oxygen partial pressure of $4x10^{-4}$ mbar employing RF magnetron sputtering technique. The effect of substrate temperature on structural, morphological, electrical and optical properties of the MoO_3 films was systematically studied. X-ray diffraction studies revealed that the films formed at 303 K were amorphous in nature, while those deposited at substrate temperature 473 K were orthorhombic MoO_3 with crystallite size of 27 nm and the crystallinity increased with increase of substrate temperature. The scanning electron micrographs of the films deposited at 303 K were of fine grain structure in amorphous back ground and the films formed at 523 K contained the grains with shape of platelets piled one over the other with size of about 1 μm. Fourier transform infrared transmittance spectra exhibited the characteristic vibration modes of MoO_3. The electrical resistivity of the films decreased with increase of substrate temperature due to partial filling of oxygen ion vacancies. The optical band gap and refractive index of the films increased with the increase of substrate temperature. The MoO_3 films formed at substrate temperature of 523 K exhibits high optical modulation of 22% and coloration efficiency of 30 cm^2/C.

Keywords

Molybdenum Oxide Films; RF Magnetron Sputtering; Substrate Temperature; Structural; Electrochromic Properties

Introduction

Transition metal oxides are semiconductors and have many technological applications in different fields such as lithium secondary batteries, display devices, optical smart windows, low cost electrochromic devices and gas sensors [Granqvist 1995, Julien 1994]. Molybdenum oxide (MoO_3), one among the transition metal oxides, exhibits interesting structural, chemical and optical properties. An orthorhombic α- phase MoO_3 layered structure is potential for lithium batteries and optical smart windows [Li et al. 2006]. Molybdenum oxide is good electrochromic material since it has oxygen deficient perovskite structure (α- and β- phases) which is suitable for intercalation and de-intercalation due to polyvalent oxidation states, which leads to bluish coloration. It also exhibits photo- and gasochromic (coloration) effects by virtue of which the material is of potential for the development of electronic display devices [Patil et al. 2008, Prasad et al. 2003, Scarminio et al. 1997]. Nanocrystalline MoO_3 films also find applications in nanodevices and nanosensors [Patzke et al. 2004, Taurino et al. 2006]. It is a promising candidate for a back contact layer for cadmium telluride solar cells in superstrate configuration due to its high work function, which reduces the contact barrier [Gretener et al. 2013]. Various physical thin film deposition techniques such as electron beam evaporation [Sabhapathi et al. 1995, Sivakumar et al. 2007], pulsed laser deposition [Ramana et al. 2007, Ramana et al. 2006], thermal evaporation [Sain et al. 2005 Yang et al. 2009] and sputtering [Okumu et al. 2006, Mahamed et al . 2007, Uthanna et al. 2010, Srinivasa Rao et al. 2009, Navas et al. 2009], and chemical methods such as spray pyrolysis [Boudaoud et al. 2006, Martinez et al. 2013], electrodeposition [Patil et al. 2006], sol-gel process [Dhanasankar et al. 2011, Fan et al. 2011] and chemical vapor deposition [Itoh et al. 2008] were used for the growth of MoO_3 films. Magnetron sputter deposition is an industrially practiced technique for deposition of oxide films. The physical properties of the sputter

deposited MoO_3 films depend critically on the sputter parameters such as oxygen partial pressure, substrate temperature, sputter power, sputter pressure and post-deposition heat treatment. In our earlier investigation, α-phase MoO_3 films were grown by thermal oxidation of DC magnetron sputtered metallic molybdenum films and their electrochemical and electrochromic properties were studied[Madhavi et al. 2013]. In the present investigation, thin films of MoO_3 were formed by RF magnetron sputtering technique at different of substrate temperatures and study their structure, surface morphology, electrical and optical properties. The electrochromic response of the MOO_3 films was studied and reported.

Experimental

Preparation And Characterization Of Moo3 Thin Films

MoO_3 thin films were deposited onto glass and silicon substrates held at different temperatures in the range 303-573 K by sputtering of pure metallic molybdenum target in oxygen and argon gas mixture using reactive RF magnetron sputtering technique. Metallic molybdenum target (99.999% pure) with 50 mm diameter and 3 mm thickness was used for sputtering. The sputter chamber was evacuated by employing diffusion pump and rotary pump combination to achieve base pressure of $4x10^{-6}$ mbar. Pressure in the sputter chamber was measured with digital Pirani – Penning gauges. After achieving base pressure of $4x10^{-6}$ mbar, oxygen gas was admitted in to the sputter chamber to the pressures in the range from $8x10^{-5}$ mbar to $8x10^{-4}$ mbar. Later, argon gas was admitted to the sputter pressure of $4x\ 10^{-2}$ mbar. The required quantities of oxygen and argon gases were admitted into the sputter chamber through fine controlled needle valves followed by Aalborg mass flow controllers (Model GFC 17). RF power of 150 W was supplied to the sputter target using RF power generator (Advance Energy Model ATX-600 W) for deposition of MoO_3 films. The sputter parameters fixed during the growth of the MoO_3 films are given in table 1.

The deposited MoO_3 films were characterized by studying their chemical composition, crystallographic structure and surface morphology, chemical binding configuration, electrical and optical properties. The thickness of the deposited films was measured with a mechanical Veeco Dektak (Model 150) depth profilometer. The chemical composition of the films was analysed with energy dispersive X-ray Analysis (Oxford instruments Inca Penta FETx3) attached to a scanning electron microscope (Carl Zeiss, model EVO MA15). The crystallographic structure of the films was determined by using X-ray diffractometer (Bruker D8 Advance Diffractometer) with copper Kα radiation with wavelength of λ = 0.15406 nm. The X-ray diffraction profiles were taken for a 2θ range between 10 and 60^0 in steps of 0.05^0. The surface morphology of the films was analysed with scanning electron microscope (Hitachi SEM Model S-400). The chemical binding configuration of the films formed on silicon substrates was analyzed with Fourier transform infrared spectrophotometer (Nicolet Magana IR 750) and recorded the optical transmittance in the wavenumber range 400–1500 cm^{-1}. The electrical resistivity of the films was measured with four point probe method. The optical transmittance of the films formed on glass substrates was recorded using UV-Vis-NIR double beam spectrophotometer (Perkin - Elmer Spectrophotometer Lambda 950) in the wavelength range 300 - 1500 nm.

TABLE 1. SPUTTER PARAMETERS FIXED DURING THE GROWTH OF MOO3 FILMS

Sputter target	: Molybdenum
Target to substrate distance	: 65 mm
Base pressure	: $4x10^{-6}$ mbar
Oxygen partial pressure (pO_2)	: $8x10^{-4}$ - $8x10^{-4}$ mbar
Substrate temperature (T_s)	: 303 - 573 K
Sputtering pressure	: $4x10^{-2}$ mbar
Sputter power	: 150 W
Deposition time	: 120 min

Results And Discussion

In oder to optimise the oxygen partial pressure for the growth of the films, the MoO_3 films were deposited at different oxygen partial pressures in the range $8x10^{-4}$ - $8x10^{-4}$ mbar. The chemical composition of the deposited films was determined by using EDAX. Figure 1 shows the representative energy dispersive X-ray analysis spectrum of the film formed a oxygen partial pressure of $4x10^{-4}$ mbar. The spectrum contained the characteristic constituent of molybdenum and oxygen in the films. The chemical constituents present in the films formed at different oxygen partial pressures are shown in table 2.

It is seen from the table that the films formed at low oxygen partial partial pressure of $8x10^{-5}$ mbar contained less quantity of oxygen than the required to form compound of MoO_3. As the oxygen partial

pressure increased to $4x10^{-4}$ mbar the films exhibited the atomic ratio of 3.02 : 1. It revealed that the oxygen partial pressure of $4x10^{-4}$ mbar is an optimum to produce nearly stiochiometric MoO_3 films. Hence an oxygen partial pressure of $4x10^{-4}$ mbar was fixed to form the films at different substrate temperatures in order to investigate their physical properties.

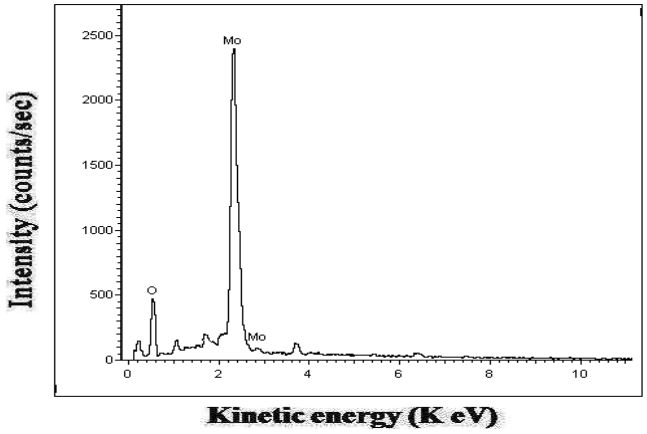

FIG. 1 EDAX SPECTRUM OF MoO3 FILM FORMED AT OXYGEN PARTIAL PRESSURE OF 4X10-4 mbar

TABLE 2 CHEMICAL COMPOSITION OF MOO3 FILMS FORMED AT DIFFERENT OXYGEN OARTIAL PRESSURES

pO_2 (mbar)	Mo (at %)	O (at %)	Mo / O
$8x10^{-5}$	79.2	20.8	3.80
$2x10^{-4}$	76.4	23.6	3.23
$4x10^{-4}$	75.2	24.8	3.03

Deposition Rate

Substrate temperature has significant influence on the thickness of the deposited MoO_3 films. The thickness of the deposited films was in the range 1.94 - 2.29 μm. Figure 2 shows the dependence of deposition rate on the substrate temperature of the MoO_3 films.

The deposition rate of the films formed at room temperature (303 K) was 16.2 nm/min. As the substrate temperature increased from 473 K to 523 K, the deposition rate increased from 18.5 nm/min to 19.1 nm/min respectively. Due to the films formed at higher substrate temperature of 573 K, there was a slight decrease in the deposition rate to 18.3 nm/min. It is noted that the formation of oxide phase during reactive sputtering occurs almost nearly substrate surface where the rate of reaction increases with increase of substrate temperature, hence leading to the higher deposition rate. Further increase of substrate temperature to 573 K resulted in a slight decrease in the deposition rate to 16 nm/min. The decrease of deposition rate at higher substrate temperatures may be due to the balance between the number of sputtered species arriving on the substrate surface and the species leaving from the substrate surface due to the re-evaporation of the deposited film hence decrease in the deposition rate.

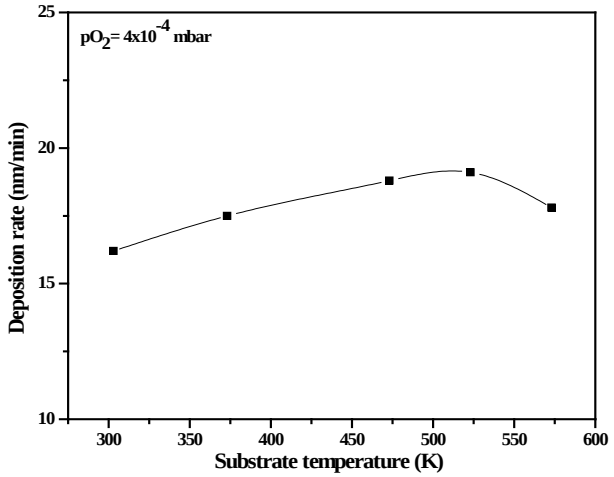

FIG. 2 VARIATION IN THE DEPOSITION RATE OF MoO3 FILMS WITH SUBSTRATE TEMPERATURE

Structural Studies

Figure 3 shows the X-ray diffraction profiles of MoO_3 films formed at different substrate temperatures. The films deposited at room temperature didn't contain the characteristic diffraction reflections of MoO_3, which revealed that the grown films were of X-ray amorphous. The films grown at substrate temperature of 473 K showed the diffraction peaks at $2\theta = 12.8^0$ and 26.3^0. These peaks were related to the (020) and (040) reflections of orthorhombic α- phase MoO_3. The presence of (020) reflections revealed the growth of layer structured α- phase MoO_3.

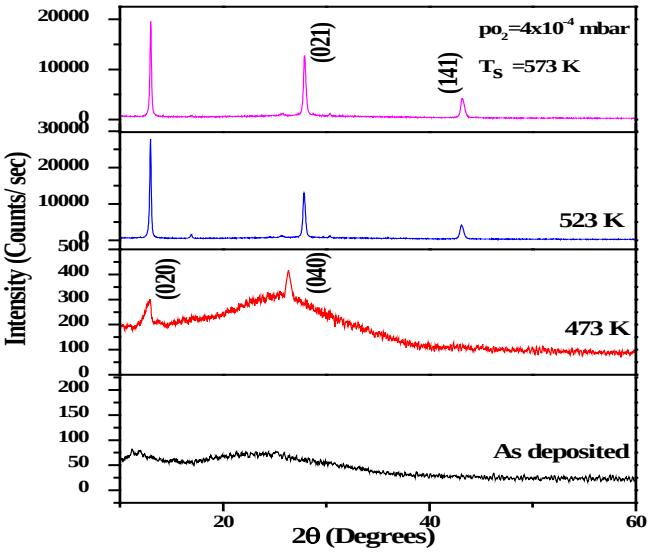

FIG. 3 XRD PROFILES OF MoO3 FILMS DEPOSITED AT DIFFERENT SUBSTRATE TEMPERATURES

The films formed at the substrate temperature of 523 K showed the diffraction peaks at $2\theta = 12.9^0$ related to the (020) reflection, 27.8^0 connected to (021) reflection and 43.2^0 for the (141) reflections of α- phase MoO_3 [JCPDS Code No. 76 – 1003]. It is noted that the (040) reflection was disappeared at substrate temperature of 523 K. The intensity of diffraction peaks increased with increase of substrate temperature revealed the improvement in the crystallinity of the films. Due to the further increase of the substrate temperature to 573 K, the decrease in the intensity of diffraction peaks indicated the decrease in the crystallinity of the films. The decrease in the crystallinity at higher substrate temperature of 573 K may be due to the higher surface mobility of adatoms on the substrate which was thermally induced, hence the reduction in the crystallinity of the deposited MoO_3 films. In the literature, Bouzidi et al. [2003] achieved α- phase MoO_3 films by spray pyrolysis in the substrate temperatures range 523 - 573 K. Such a layered structured MoO_3 films were achieved by Martinez et al. [2013] at substrate temperature range from 473 to 673 K by spray deposition. It is noted that Sivakumar et al. [2007] obtained α- phase MoO_3 films at low substrate temperature of 473 K in electron beam evaporation. Yang et al. [2009] found that the mixed α- and β- phase MoO_3 films in electron beam deposition. It was clearly indicated that the grown crystallographic structure of the MoO_3 films mainly depends on the substrate temperature and the method of film growth.

The crystallite size (L) of the films was calculated from the X-ray diffraction peaks of (020) by using Debye - Scherrer's relation [Cullity, 1974]

$$L = 0.89\lambda / \beta \cos\theta \quad \text{---------- (1)}$$

where λ is the wavelength of the X-rays (0.15406 nm), β the full width at half maximum of diffraction intensity measured in radians and θ the diffraction angle. Figure 4 shows the variation of crystallite size of MoO_3 films with substrate temperature. The full width at half maximum of the peak (020) in the films decreased from 0.20^0 to 0.14^0 with increase of substrate temperature from 473 K to 523 K respectively. In terms of the further increase of substrate temperature to 573 K, it increased to 0.19^0. The crystallite size of the MoO_3 films deposited at substrate temperature of 473 K was 27 nm. As the substrate temperature increased to 523 K, the crystallite size increased to 62 nm. At higher substrate temperature of 573 K, the crystallite size decreased to 43 nm. The crystallite size of the films increased with increase of substrate temperature upto 523 K. At 523 K, the XRD shows that intensity of (0k0) reflection is maximum, indicating the layered structure of MoO_3. On further increment of substrate temperature to 573 K the intensity of (0k0) reflection decreased and intensity of peaks (021) and (141) increased. It revealed that though the films at higher substrate temperature of 573 K were not of layer structured α- phase MoO_3. At higher substrate temperature of 573 K, the crystallite size decreased to 43 nm due to the re-evaporation hence smaller size of crystallites was grown.

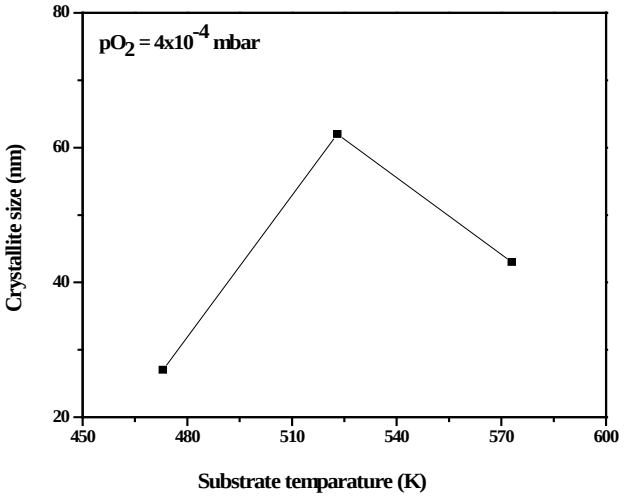

FIG. 4 VARIATION OF CRYSTALLITE SIZE OF MoO3 FILMS WITH SUBSTRATE TEMPERATURE

In literature, Martinez et al. [2013] reported that the crystallite size decreased from 30 nm to 10 nm with increase of substrate temperature from 423 K to 553 K respectively in the MoO_3 films formed by spray pyrolysis method. Fan et al. [2011] also noticed the decrease in the crystallite size from 32 nm to 25 nm with increase of substrate temperature from 573 K to 673 K in RF sputtered MoO_3 films.

Figure 5 shows the dependence of interplanar spacing $d_{(020)}$ on the substrate temperature of the MoO_3 films. It was seen from the figure that the interplanar $d_{(020)}$ spacing decreased from 0.337 nm to 0.314 nm with increase of substrate temperature from 473 K to 573 K respectively. The decrease in the interplanar spacing with increase of substrate temperature was mainly due to compressive stresses developed in the films.

The dislocation density (δ) and strain (ε) developed in the films were calculated from the crystallite size using the relations,

Dislocation density, $\delta = 1/L^2$ ---------- (2)

Figure 6 shows the variation of dislocation density

developed in the MoO_3 films with substrate temperature. The dislocation density of the films deposited at substrate temperature of 473 K was $1.4x10^{15}$ lines/m^2 and it decreased to $2.6x10^{14}$ lines/m^2 at substrate temperature of 523 K. On further increase of substrate temperature to 573 K, the dislocation density increased to $5.4x10^{14}$ lines/m^2.

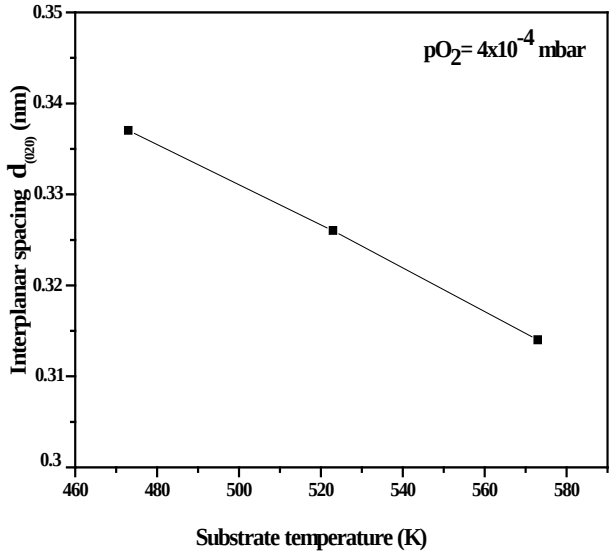

FIG. 5 VARIATION IN THE INTER PLANAR d(020) SPACING OF MoO3 FILMS WITH SUBSTRATE TEMPERATURE

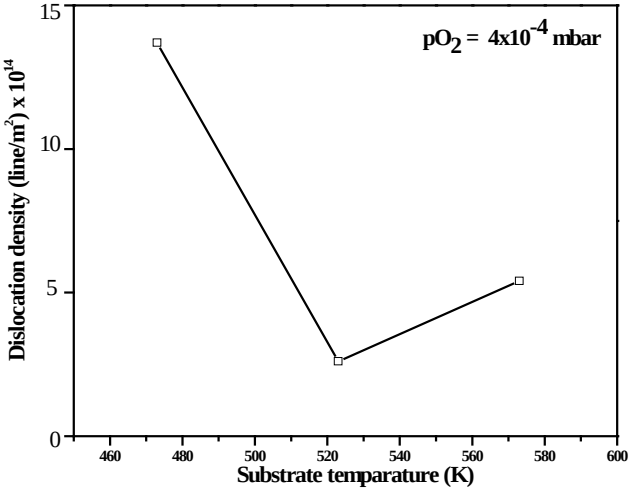

FIG. 6 DEPENDENCE OF DISLOCATION DENSITY OF MoO3 FILMS ON SUBSTRATE TEMPERATURE

The decrease in dislocation density in the films were mainly due to the enhancement in the crystallinity with increase of substrate temperature up to 523 K. At higher substrate temperature of 573 K there was a increase in the dislocation density and strain in the films.

Stress (σ) developed in the films was estimated from lattice parameter using the relation [Eckertova, 1984],

Stress, $\sigma = Y[(a - ao) /2 \nu ao]$ ---------- (3)

where a is the experimentally determined lattice parameter, ao the bulk lattice parameter, ν the Poisson's ratio and Y the Young's modulus.

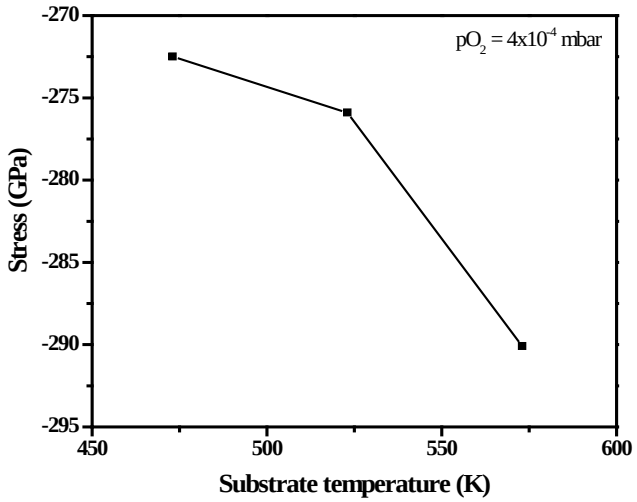

FIG. 7 VARIATION OF STRESS WITH SUBSTRATE TEMPERATURE

Figure 7 shows the variation of stress in MoO_3 with substrate temperature. It is seen from the figure that the stress in the films decresed from -273 to -290 GPa with increase of with increase of substrate temperature from 473 to 573 K respectively. The decrease of stress with increase of substrate temperature clearly indicated that the compressive stress decreased with the increase of substrate temperature.

Surface Morphology

The surface morphology of the deposited MoO_3 films was analyzed with scanning electron microscope. Figure 8 shows the scanning electron microscope images of the films formed at different substrate temperatures. SEM images of MoO_3 films formed at room temperature (303 K) showed very smooth morphology without any fragmentation features or topographical contrast, which indicated the growth of fine grain structure in amorphous background. The average size of the grown grains were of about 150 - 200 nm. The films deposited at substrate temperature of 473 K showed the grain growth with the shape of needle or elongated thin long bar structures. The size of grown grain size was of about 800 nm long and 150 nm in diameter. At this substrate temperature, the crystallinity of the films was increased due to the coalescence of neighbour crystallites driven by thermal energy received from the substrate by heating. Further increase of substrate temperature to 523 K the growth of grains like platelets piled one over the other with size of about 1 μm to 1.5 μm. The films formed at

higher substrate of 573 K the size of the grains decreased to about 1.2 μm. In general, the MoO_3 films grew with grains in the shape of needles platelets, elongated columns and rectangular shape depend on the deposition method employed and process parameters maintained during the deposition. Hence, the observed needle and platelet shaped grains achieved at higher substrate temperatures may be due to better mobility of adatoms or molecules to promote the growth. Yang et al. [2009] noticed the grains with pearl-like structure with platelets one over the other with size varied from 0.1 μm to 4 μm at substrate temperature of 373 K while at higher temperature of 673 K the average diameter of nanocrystallites of about 0.1 μm diameter and 3.5 μm long in electron beam evaporated MoO_3 films. The grains with shape of platelets were also grown by Wu et al. [2009] in vapor transport deposited MoO_3 films. Comini et al. [2008] achieved needle like nanoparticles with size about 200-400 nm at substrate temperature of 973 K in sol-gel deposited films.

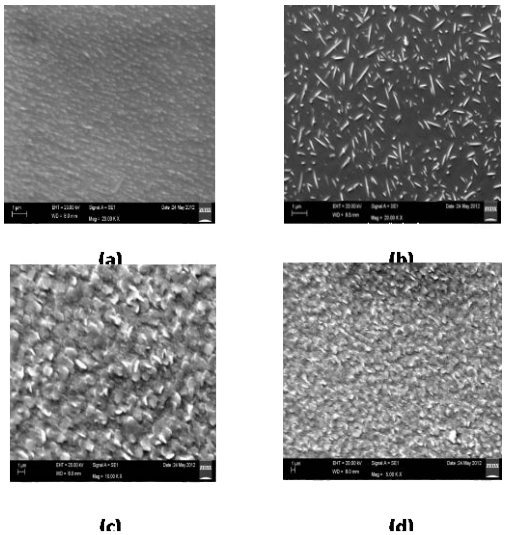

FIG. 8 SEM IMAGES OF MoO3 FILMS FORMED AT DIFFERENT SUBSTRATE TEMPERATURES: a) 303 K, b) 473 K, c) 523 K AND d) 573 K

Fourier Transform Infrared Spectroscopy

The infrared spectroscopy gives the information about the chemical binding of the atoms in the deposited films. Figure 9 shows Fourier transforms infrared transmittance spectra of MoO_3 films formed at different substrate temperatures. The films formed at 303 K showed a broad absorption band between 600 cm^{-1} and 1000 cm^{-1} which is the characteristic Mo - O vibrations attributed to the wide range of bands with different angles and lengths in the amorphous nature.

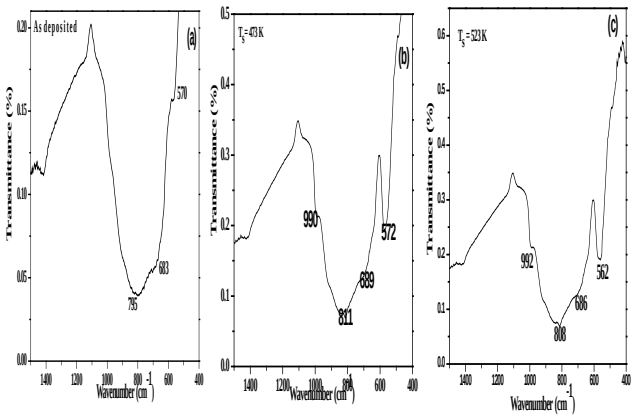

FIG. 9 FTIR TRANSMITTANCE SPECTRA OF MoO3 FILMS FORMED AT DIFFERENT SUBSTRATE TEMPERATURES : a) 303 K, b) 473 K AND c) 523 K

There were three weak absorption bands around 795 cm^{-1}, 668 cm^{-1} and 570 cm^{-1} related to two stretching vibration modes of Mo = O, Mo - O and one transverse optical vibrations mode of Mo - O - Mo respectively [Navas et al. 2009]. The FTIR spectra of the films formed at substrate temperature 473 K showed the absorption bands at about 990 cm^{-1}, 811 cm^{-1}, 689 cm^{-1} and 572 cm^{-1}. The absorption band observed at 811 cm^{-1} was attributed to the bridging vibration of Mo = O indicated the existence of Mo^{6+} oxidation state related to α- phase MoO_3 and 992 cm^{-1} for stretching mode of Mo = O. Further increase of substrate temperature of 523 K, the intense absorption band observed at 567 cm^{-1} along with weak bands at 686 cm^{-1}, 808 cm^{-1} and 992 cm^{-1}. The absorption band seen at 567 cm^{-1} was assigned to the bending vibration of Mo - O - Mo bond, the broader band at around 808 cm^{-1} attributed to the binding vibrations of Mo^{6+} which shifted to lower wavenumber side. Nazri and Julien [1992] observed the terminal oxygen stretching mode (ν) of M = O and the bending vibrational mode of Mo - O - Mo at 988 cm^{-1} and 687 cm^{-1} respectively in heat treated MoO_3 films.

Electrical Properties

Figure 10 shows the variation of electrical resistivity of MoO_3 films with substrate temperature. The electrical resistivity of the films increased with increase of substrate temperature. The films formed at room temperature exhibited low electrical resistivity of $1.2x10^3$ Ωcm. The low electrical resistivity of films was due to amorphous nature and presence of oxygen ion vacancies. The electrical resistivity increased from $1.6x10^4$ Ωcm to $3.4x10^4$ Ωcm with increase of substrate temperature from 473 K to 523 K. The increase in resistivity with substrate temperature was due to the

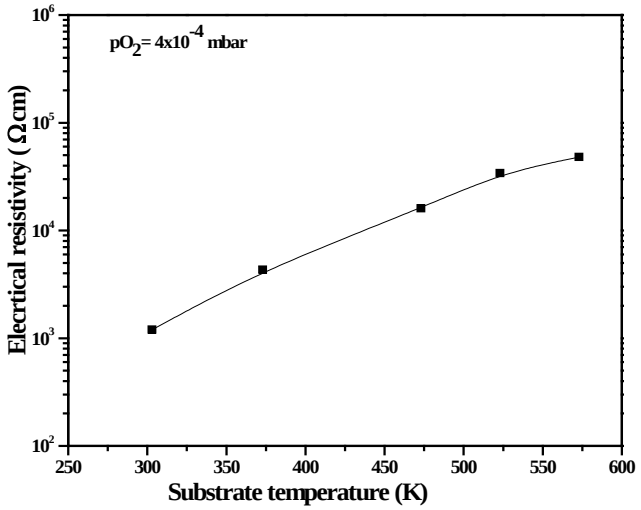

FIG. 10 VARIATION IN ELECTRICAL RESISTIVITY OF MoO3 FILMS WITH SUBSTRATE TEMPERATURE

polycrystalline nature of the films as well as filling the oxygen ion vacancies. At higher substrate temperature of 573 K the electrical resistivity further increased to 4.8x104 Ωcm. In the literature, Sabhapathi et al. [1995] achieved the electrical resistivity of 5x104 Ωcm at Substrate temperature of 573 K in electron beam evaporated MoO_3 films. Yang et al. [2009] reported the electrical resistivity of the films formed at substrate temperatures 373 K and 473 K were higher than those formed at substrate temperature of 573 K and 673 K, which was due to the presence of different phase of the structure. Yahaya et al. [1998] achieved high electrical resistivity of $3x10^6$ Ωcm at substrate temperature of 373 K, later decreased with increase of substrate temperature or annealing in air in electron beam deposited MoO_3 films. But in vacuum evaporated MoO_3 films, the electrical resistivity decreased from $1x10^{10}$ Ωcm to $5x10^4$ Ωcm with increase of substrate temperature from 323 K to 673 K respectively. Boudaoud et al. [2006] reported the electrical resistivity of $4x10^5$ Ωcm in spray deposited films formed at substrate temperature of 423 K. Miyata and Akiyashi [1985] reported the highest electrical resistivity of $2x10^{10}$ Ωcm in RF magnetron sputtered films. It is noted that the electrical resistivity of the DC magnetron sputtered MoO_3 films increased from $3.3x10^3$ Ωcm to $8.3x10^4$ Ωcm with increase of substrate temperature from 303 K to 473 K respectively.

Optical Properties

The optical absorption in the MoO_3 films was influenced by the substrate temperature. Figure 11 shows the optical transmittance spectra of MoO_3 films formed at different substrate temperatures in the range 303 - 573 K. The films formed at 303 K showed an average optical transmittance of about 60% at wavelengths higher than 600 nm. As the substrate temperature of the films increased to 523 K the transmittance of the films increased to 85%. High optical transmittance of the films formed at this substrate temperature was due to the decrease in the oxygen ion vacancies in the films. The films formed at higher substrate temperature of 573 K exhibited a decrease in the optical transmittance. The optical absorption edge of the films shifted to lower wavelength side with increase of substrate temperature up to 523 K and at higher substrate temperature of 573 K, the absorption edge shifted to red side. The red shift in the absorption edge at higher substrate temperature was due to the scattering of photons by the charge carriers.

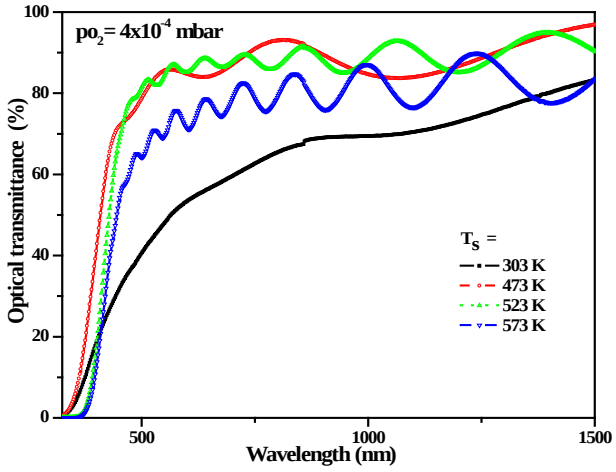

FIG. 11 OPTICAL TRANSMITTANCE OF MoO3 FILMS DEPOSITED AT DIFFERENT SUBSTRATE TEMPERATURES

The optical absorption coefficient (α) of the films was evaluated from the optical transmittance (T) data using the relation,

$$\alpha = - (1/t) \ln (T) \quad (4)$$

where t is the film thickness. The optical band gap (E_g) of the films was evaluated from the optical absorption coefficient using the Tauc's relation [Tauc, 1974] assuming that the direct transitions takes place in these films.

$$(\alpha h\upsilon) = A (h\upsilon - E_g)^2 \quad (5)$$

The optical band gap of the films was determined from the plot of $(\alpha h\upsilon)^2$ versus photon energy ($h\upsilon$). The extrapolation of the linear portion of plots of $(\alpha h\upsilon)^2$ versus photon energy to $\alpha = 0$ yield the optical band gap of the films. The optical band gap of the films increased from 2.98 eV to 3.28 eV with increase of substrate temperature from 303 K to 473 K respectively. On further increase of substrate

temperature to 523 K, the optical band gap increased to 3.34 eV, there after it decreased to 3.22 eV at higher substrate temperature of 573 K. It is to be noted in the literature that the optical band gap decreased from 2.80 eV to 2.35 eV with increase of substrate temperature from 303 K to 473 K in the MoO_3 films formed on glass substrates while those formed on FTO coated glass decrease from 2.76 eV to 2.30 eV with increase of substrate temperature from 303 K to 473 K in electron beam evaporated films [Boudaoud et al. 2006]. Sabhapathi et al. [1995] noticed such a decrease in the optical band gap with increase of substrate temperature in electron beam deposited films. Ramana and Julien. [2006] found that the optical band gap decreased from 3.35 eV to 2.81 eV with increase of substrate temperature from 303 K to 773 K in pulsed laser deposited films. Recently, Navas et al. [2009] observed the increase in the optical band gap from 3.35 eV to 3.62 eV with increase of annealing temperature from 473 K to 673 K in RF magnetron sputtered MoO_3 films. A large optical band gap value of 3.93 eV was achieved by Lin et al. [2009] in electron beam evaporated films. The optical band gap of the films increased from 2.98 eV to 3.34 eV with increase of substrate temperature from 303 K to 523 K respectively. This is due to the reduction of oxygen deficiency and the stoichiometric approach of film composition [Elangovan et al. 2009].The band gap decreased for substrate temperature higher than 523 K, the oxygen vacancies occupied by electrons generate energy levels in the energy gap, which is close to valence band and act as donor canters. These oxygen vacancies which form a defect band in forbidden band are responsible for the broad-band absorption. [Deb and Chopoorian. 1996, Sian and Reddy. 2004, Yang et al. 2009].

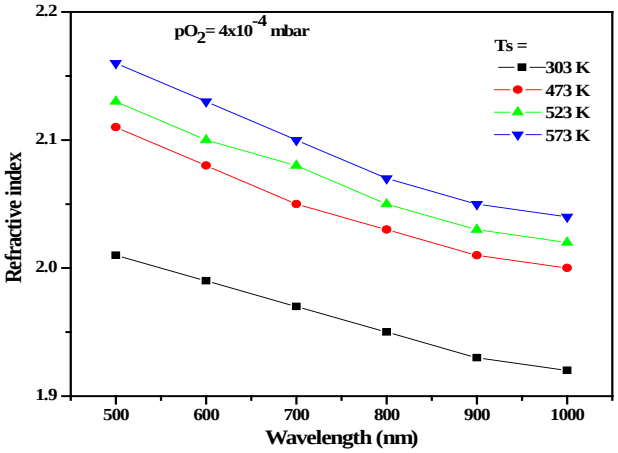

FIG. 12 WAVELENGTH DEPENDENCE REFRACTIVE INDEX OF MoO3 FILMS

Figure 12 shows the variation of refractive index with wavelength of MoO_3 films formed at different substrate temperatures. In general, the refractive index of MoO_3 films decreased with increase of wavelength. The refractive index of the films at 500 nm at room temperature was 2.01 and at substrate temperature of 473 K it was increased to 2.11. The low value of refractive index at 303 K was due to the low packing density because of the amorphous nature of the films. On increase of substrate temperature from 523 K to 573 K, the refractive index of the films increased from 2.13 to 2.16. The increase in the refractive index with increase of substrate temperature was due to improvement in the crystallinity and the packing density of the films. Uthanna et al. [2010] observed that the refractive index of the DC magnetron sputtered MoO_3 films increased from 2.03 to 2.10 with increase of substrate temperature from 303 K to 573 K.

Electrochromic Properties

Figure 13 shows the optical transmittance spectra of colored and virgin (bleached) states of the MoO_3 films formed at 303 K and 523 K. The optical modulation, (ΔT %) is the difference of transmittance T_b in bleached and T_c in colored state [(T_b% $_{bleached}$) – (T_c% $_{colored}$)]. The color efficiency (η) at a particular wavelength correlated to the optical contrast can be given by the relation [Granqvist, 1995],

$$\eta = \log (T_b/T_c) / (Q/A) = (\Delta OD) / (Q/A) \qquad (6)$$

where T_b is the bleaching state transmittance, T_c the colored state transmittance, Q the charge inserted into the films and A the area of the films.

The films formed at 303 K showed the virgin state optical transmittance of 53% where as in the colored state it decreased to 38%. The films prepared at 303 K exhibited the optical modulation (at 600 nm), ΔT = 15%. The color efficiency of these MoO_3 films was 26 cm^2/C. On increasing the substrate temperature to 523 K, the optical transmittance of the virgin state was 87% and at colored state it decreased to 65% with optical modulation of 22%. The color efficiency of the MoO_3 films formed at substrate temperature 523 K was increased 30 cm^2/C. Thus the optical modulation and coloration efficiency was increase with increase of substrate temperature from 303 K to 523 K. The coloration efficiency of the films deposited at 573 K decreased to 24 cm^2/C. The decrease in the coloration efficiency at higher substrate temperature of 573 K may be due to the decrease in the intercalation of Li+ ions during the coloration process. Lin et al. [2010]

reported the coloration efficiency of 25.1 cm^2/C for the films annealed at 573 K. Recently, Madhavi et al. [2013] achieved the optical modulation of 14% and coloration efficiency of 27 cm^2/C in thermally oxidized MoO_3 films. Sivakumar et al. [2006] reported a maximum coloration efficiency of 30 cm^2/C at the wavelength of 633 nm in the films formed at room temperature and it decreased to 14 cm^2/C in the films formed at substrate temperature of 473 K, there after it increased to 22 cm^2/C at 573 K in electron beam evaporated MoO_3 films. The films deposited at 523 K exhibited the better electrochromic properties which will be useful in manufacturing of electrochromism based smart windows.

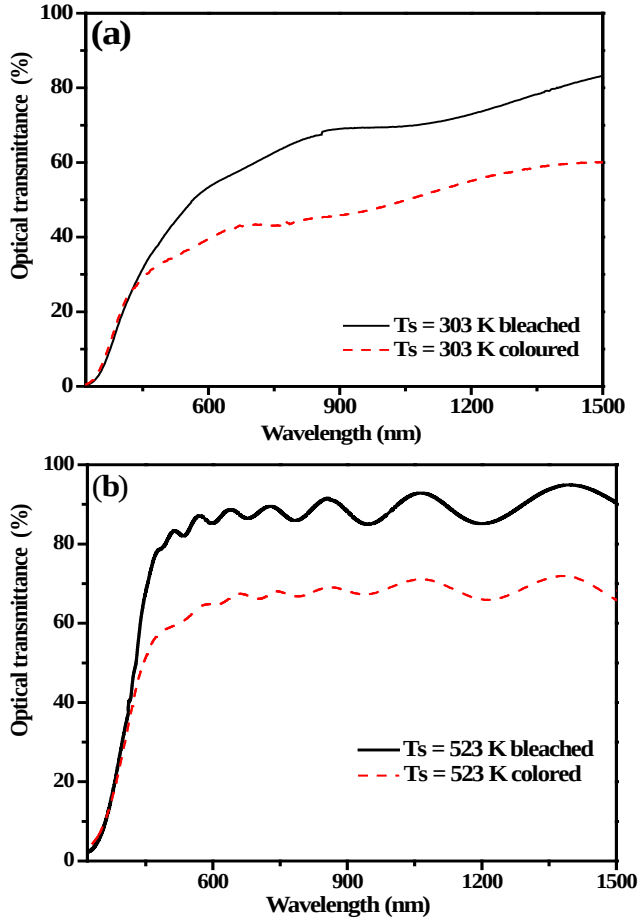

FIG. 13 OPTICAL TRANSMITTANCE SPECTRA OF COLORED AND BLEACHED STATE OF MOO3 FILMS FORMED AT SUBSTRATE TEMPERATURES: a) 303 K AND b) 523 K

Conclusions

Thin films of molybdenum oxide were formed on glass and silicon substrates by RF magnetron sputtering of metallic molybdenum target at varying substrate temperatures in the range 303 – 573 K. The deposited films were characterized for their crystallographic structure by X-ray diffraction, surface morphology with scanning electron microscope and chemical binding configuration by fourier transform infrared spectroscopy. The electrical and optical properties were studied using appropriate methods. The influence of substrate temperature on the structural and surface morphology, electrical and optical properties of the MoO_3 films was systematically investigated. The films formed at room temperature (303 K) were X-ray amorphous, and the films formed at 473 K showed the (020) and (040) reflections indicating the growth of α- phase MoO_3. The crystallite size of the films increased from 27 nm to 62 nm with increase of substrate temperature. The scanning electron microscope images indicated that the films formed at 303 K were of smooth surface morphology and fine grain structure in amorphous background. The films deposited at substrate temperature of 523 K exhibited the growth of grains with shape of platelets piled one over the other about the size of 1 μm to 1.5 μm. Fourier transform infrared transmittance spectrum of the films formed at 303 K showed broad absorption band between 600 and 1000 cm^{-1} associated with the charecteristic Mo-O vibrations in the amorphous background. The films formed at 473 K exhibited the bridging and stretching vibrations of Mo = O confirmed the existence of Mo^{6+} oxidation state related to of phase MoO_3. The electrical resistance of the amorphous MoO_3 films formed at 303 K was $1.2x10^3$ Ωcm and at substrate temperature of 523 K it increased to $3.4x10^4$ Ωcm due to the crystalline nature as well as filling of oxygen ion vacancies. The optical band gap of the films increased from 2.98 eV to 3.34 eV with increase of substrate temperature from 303 K to 523 K. The refractive index of the films increased with increase of substrate temperature due to improvement in the crystallinity and packing density of the films. The electro chromic performance of the films was studied on the MoO_3 films. Optical modulation of the films increased from 15% to 22% and coloration efficiency increased from 26 cm^2/C to 30 cm^2/C with increase of substrate temperature from 303 K to 523 K respectively.

REFERENCES

Boudaoud, L.; Benramdana, N.; Desfeux, R.; Khalifa. and B. Mathieu, C. "Structural and Optical properties of MoO_3 and V_2O_5 thin films prepared by spray pyrolysis", Catal. Today, vol 113, 2006, pp. 230.

Bouzidi, A., Benramdane, N., Derraz, H.T., Mathieu, C., Khelifa, B. and Desfeux, R., "Effect of substrate

temperature on the structural and optical properties of MoO_3 thin films prepared by spray pyrolysis technique", Mater. Sci. Eng. B, vol 97, 2003, pp. 5.

Comini, E., Foglia, G., Sherveglieri, G., Cantalini, C., Passacantano, M., Santace, S., Li, Y., Wlodarski, W. and Qu, W., "Carbon monoxide response of molybdenum oxide thin films deposited by different techniques", Sens. Actuators B, vol 68, 2008, pp. 168.

Cullity, B.D., Elements of X-ray Diffraction, IInd Ed, Addison Wesley, London. 1978.

Deb, S.K. and Chopoorian, J.A., "Optical properties and color-center formation in thin films of molybdenum trioxide", J. Appl. Phys., vol 37, 1966, pp. 4818.

Dhanasankar, M.; Purushothaman, K.K. and Muralidharan, G.,"Effect of temperature and annealing on optical, structural and electro-chromic properties of sol–gel dip coated molybdenum oxide films," Appl. Surf. Sci., vol 257, 2011, pp. 2074.

Eckertova, L., "Physics of Thin Films" Plenum Press, New York, 1984.

Elangovan, E., Goncalves, G., Martins, R., Fortunato, E.," RF sputtered wide work function indium molybdenum oxide thin films for solar cell applications," Solar Energy, vol 83, 2009, pp. 726.

Fan, X., Fang, G., Qin, P., Sun, N., Liu, N., Zheng, Q., Cheng, F., Yuan, L. and Zhao, X., "Deposition temperature effect of RF magnetron sputtered molybdenum oxide films on the power conversion efficiency of bulk- heterojunction solar cells", J. Phys. D: Appl. Phys., vol 44, 2011, pp. 045101.

Ghosh, S., Avasthi, D.K., Shah, P., Ganesan, V., Gupta, A., Sarangi, D., Bhattacharya, R. and Assmann, W.,"Deposition of thin films of different oxides of copper by RF reactive sputtering and their characterization" Vacuum, Vol 57,2000, pp 377.

Granqvist C.G., Handbook of Inorganic Electro-chromic Materials, Elsevier, Amsterdam, 1995.

Granqvist, C.G., "Electrochromic tungsten oxide films: Review of progress 1993–1998," Solar Energy Mater. Solar Cells, vol 60, 2000, pp. 201.

Gretener, C.; Perrenoud, J.; Kranz, L.; Baechler, C.; Yoon, S.; Romanyuk, Y.E.; Buecheler, S. and Tiwari, A.N. "Development of MoOx thin films As back contact buffer for CdTe solar cells in substrate configuration", Thin Solid Films , vol 535, 2013, pp. 193.

Itoh, T., Matsubara, I., Shin, W., Izu, N. and Nishibori, M., "Preparation of layered organic– inorganic nanohybrid thin films of molybdenum trioxide with polyaniline derivatives for aldehyde gases sensors of several tens ppb level," Sens. Actuators B, vol 128, 2008, pp. 512.

Julien C. M., Pistonia (Ed), Lithium Batteries; New Materials, Developments and Perspectives, Amsterdam, North Holland, 1994.

Li, W., Cheng, F., Tao, Z and Chen, J., "Vapor-transportation preparation and reversible lithium intercalation/deintercalation of α-MoO_3 Microrods", J. Phys. Chem. B, vol 110, 2006 pp. 119.

Lin, S.Y., Wang, C.M., Kao, K.S., Chen, Y.C. and Liu, C.C. "Electrochromic properties of MoO_3 thin films derived by a sol–gel process, J. Sol- gel. Sci. Technol., vol 53, 2010, pp. 51.

Lin, S.Y.; Chen, Y.C., Wang, C.M.; Hseich, P.T.; Shih, *S.C.*,"Post-annealing effect upon optical properties of electron beam evaporated molybdenum oxide thin films", Appl. Surf. Sci., vol 255, 2009, pp. 3868.

Madhavi, V., Kondaiah, P., Subbarayudu, S., Hussain O. M. and Uthanna, S., "Properties of MoO_3 films by thermal oxidation: Annealing induced phase transition", Mater. Express, vol 3, 2013, pp. 135.

Mahamad, S.H. and Venkatraj, S., "Thermal stability of amorphous molybdenum trioxide films prepared at different oxygen partial pressures by reactive DC magnetron sputtering", Vacuum, vol 81, 2007, pp. 636.

Martinez, H.M.; Torres, J.; Lopez Correno, L.D.; Rodriguez-Garcia, M.E., "Effect of substrate temperature on the physical properties of molybdenum trioxide thin films obtained through the spray pyrolysis technique," Mater. Character., vol 25, 2013, pp. 184.

Miyata, N. and Akiyoshi, S., "Preparation and electrochromic properties of RF sputtered molybdenum oxide films," J. Appl. Phys., vol 58, 1985, pp. 1651.

Navas, I., Vinodkumar, R., Lethy, K.J., Satyanarayana, M., Ganesan, V. and Mahadevan Pillai, V.P., "Enhanced ethanol sensing response from nanostructured MoO_3", J. Nanosci. Nanotechnol., vol 9, 2009, pp. 5254.

Navas, I.; Vinod Kumar, R.; Lethy, K.J.; Detty, A.P.;

Ganesan, V.; Sathe, V. and Mahadevan Pillai, V.P. "Growth and characterization of molybdenum oxide nanorods by RF magnetron sputtering and subsequent annealing", J. Phys. D: Appl. Phys., vol 42, 2009, pp. 175305.

Nazri, G.A., and Julien, C.M.,"Far infrared and Raman studies of orthorhombic MoO_3 single crystal", Solid State Ionics, vol 53, 1992, pp. 376. Okumu, J., Koerfer, F., Salinga, C., Pedersen, T.P. and Wuttig, M., "Gasochromic switching of reactively sputtered molybdenum oxide films: A correlation between film properties and deposition pressure," Thin Solid Films, vol 515, 2006, pp. 1327.

Patil, R.S.; Uplane, M.D. and Patil, P.S. "Structural and optical properties of electro-deposited molybdenum oxide thin films," Appl. Surf. Sci., vol 252, 2006, pp. 8050.

Patil, R.S.; Uplane, M.D. and Patil, P.S., "Electro-synthesisof electrochromic molybdenum oxide thin films with rod-like features", Int. J. Electrochem. Sci., vol 3, 2008, pp. 259.

Patzke, G.R., Michailovski, A., Krumeich, F., Nesper, R., Grunwaldt, J.D. and Baiker, A., "One-step synthesis of submicrometer fibers of MoO_3, Chem. Mater., vol 16, 2004, pp. 1126.

Prasad, A.K., Kubinski, D.J. and Gouma, P.I., "Comparison of sol–gel and ion beam deposited MoO_3 thin film gas sensors for selective ammonia detection," Sens. Actuators B, vol 93, 2003, pp. 25.

Ramana, C.V. and Julien, C.M. "Chemical and electrochemical properties of molybdenum oxide thin films prepared by reactive pulsed- laser assisted deposition", Chem. Phys. Lett., vol 428, 2006, pp. 114.

Ramana, C.V., Atuchin,V V., Kesler, V. G.,Kochubey,V.A., Pokrovsky, L.D., Shutthanandan, V., Becker., U. and Ewing, R.C., "Growth and surface characterization of sputter-deposited molybdenum oxide thin films", Appl. Surf. Sci., vol. 253, 2007, pp. 5368.

Sabhapathi, V.K., Hussain, O.M., Uthanna, S., Srinivasulu Naidu, B., Jayarama Reddy, P., Julien, C. and Balkanski, M., "AC conductivity studies on Al/MoO_3/Al sandwich structures", Mater. Sci. Eng. B, vol 32, 1995, pp. 93.

Sain, T.S. and Reddy, G.B., "Stoichiometric amorphous MoO_3 films: A route to high performance electrochromic devices," J. Appl. Phys., vol *98*, 2005, pp. 026104.

Scarminio, J., Lourenco, A., and Gorenstein, A., "Electrochromism and photochromism in amorphous molybdenum oxide films," Thin Solid Films, vol 302, 1997, pp. 66.

Sian, T.S. and Reddy. G.B., "Optical, structural and photoelectron spectroscopic studies on amorphous and crystalline molybdenum oxide thin films," Solar Energy Mater. Solar Cells, vol 82, 2004, pp. 375.

Sivakumar, R., Manisankar, P., Jayachandran, M. and Sanjeeviraja, C., "Intercalation studies on electron beam evaporated MoO_3 films for electrochemical devices", Solar Energy Mater. Solar Cells, vol 90, 2006, pp. 2438.

Sivakumar, R.; Gopalakrishnan, R.; Jayachandran, M. and Sanjeeviraja, C., "Characterization on electron beam evaporated α- MoO_3 thin films by the influence of substrate temperature," Curr. Appl. Phys., vol 7, 2007, pp. 51.

Srinivasa Rao,K,; Rajini Kanth, B. andMukhopadhyay P.K., "Optical and IR studies on RF magnetron sputtered ultra-thin MoO_3 films", Appl. Phys. A, vol 9, 2009, pp. 985.

Tauc, J., "Amorphous and Liquid Semiconductors", Plenum Press, New York, 1974.

Taurino, A. M., Forleo, A., Francioso, L. and Siciliano, P., "Influence of doping on the preferen- tial growth of α-MoO", Appl. Phys. Lett., vol 88, 2006, pp. 152111.

Uthanna, S.; Nirupama, V. and Pierson, J.F. "Substrate temperature influenced structural, electrical and optical properties of dc magnetron sputtered MoO_3 films", Appl. Surf. Sci., vol 256, 2010, pp. 3133.

Wu, M.C. and Lee, C.S., "α- MoO_3 nanocrystals of controlled size on a glass substrate", Mater. Res. Bull., vol 44, 2009, pp. 629.

Yahaya, M., Salleh, M.M. and Talib, I.A., "Optical properties of MoO_3 thin films for electrochromic windows", Solid State Ionics, vol 113, 1998, pp.421.

Yang, W.Q., Wei, Z.R., Zhu, X.H. and Yang, D.Y., "Strong influence of substrate temperature on the growth of nanocrystalline MoO_3 thin films," Phys. Lett. A, vol *373*, 2009, pp. 3965.

Yang, W.Y., Kim, W.G. and Rhee, S.W., "Radio frequency

sputter deposition of single phase cuprous oxide using Cu_2O as a target material and its resistive switching properties", Thin Solid Films, Vol 517, 2008, pp. 967.

Mr. S. Subbarayudu received his Master Degree in Physics from Sri Krishnadevaraya University, Anantapur, India during the year 1991 - 93. He is working as Assistant Professor in Physics, SBVR Degree College, Badvel, Andhra Pradesh. He is carrying out research work leading to the Degree of Doctor of Philosophy in Physics in the Department of Physics, Sri Venkateswara University, Tirupati - 517 502, Andhra Pradesh, India. Currently he is working on the preparation and characterisation of RF magnetron sputtered MoO_3 films for applications in gas sensors and electrochrmic devices.